

Search for compressed mass Higgsino production with soft lepton tracks with the CMS experiment in proton-proton collision data at $\sqrt{s} = 13$ TeV

VON DER FAKULTÄT FÜR PHYSIK DER UNIVERSITÄT HAMBURG ZUR
ERLANGUNG DES AKADEMISCHEN GRADES EINES DOKTORS DER
NATURWISSENSCHAFTEN GENEHMIGTE DISSERTATION

VORGELEGT VON

YUVAL NISSAN

IM AUGUST 2022



Universität Hamburg
DER FORSCHUNG | DER LEHRE | DER BILDUNG

Abstract This is the abstract

Contents

1	Introduction	1
2	Quantum Field Theory and The Standard Model	3
2.1	Quantum Field Theory	3
2.2	The Standard Model of particle physics	3
2.2.1	The particle content	3
3	Supersymmetry	5
3.0.1	Phenomenology of Higgsino production	5
4	Multivariate Statistics	7
4.1	Decision Trees	7
5	Experimental setup	9
5.1	The Large Hadron Collider	9
5.2	The Compact Muon Solenoid experiment	9
5.3	Simulation of events	9
6	Object reconstruction and identification of particles and jets	11
6.1	Track reconstruction	11
6.2	Electrons	11
6.3	Muons	11
7	Search for compressed Higgsinos with soft lepton tracks	13
7.1	Motivation	13
7.2	Signal models	13
7.3	Previous searches	13
7.4	Search strategy	14
7.4.1	Exclusive track category	14
7.5	Signal signature and base selection	15
7.5.1	Missing Transverse Energy	15
7.5.2	Jets and hardronic activity	15
7.5.3	Base selection	16
7.5.4	Dilepton kinematics	17
7.5.5	Main drivers of sensitivity	23
7.6	Simulated samples	25
7.6.1	Standard Model simulated samples	25
7.6.2	Signal simulated samples	25
7.7	Object definition and selection	26
7.7.1	Electrons	26
7.7.2	Muons	30

7.7.3	Scale factors	34
7.7.4	Missing transverse energy	35
7.7.5	Tracks and multivariate selection	39
7.7.6	Isolation	43
7.8	Trigger	43
7.9	Event Selection	43
7.9.1	Preselection	43
7.9.2	High- p_T lepton veto	43
7.9.3	Selection Efficiencies	43
7.9.4	Boosted Decision Trees	43
7.10	Characterisation and Estimation of the Standard Model Backgrounds	43
7.11	Optimisation of Sensitivity	43
7.12	Results	43
7.13	Interpretation	43
8	Jet Isolation and Non-Isolated Background Estimation	45
8.1	Jet Isolation	45
8.1.1	Optimisation	45
8.2	Non-Isolated Background	45
9	Summary	47
10	Latex stuff	49
10.1	Some examples	49
10.1.1	Multiline comment	49
10.1.2	Fixme note	49
10.1.3	Tables	49
10.1.4	Cross References	49
10.1.5	Particles	49
10.1.6	Citing	49
10.1.7	Glossary	49
10.1.8	Acronyms	50
	Glossary	53
	Acronyms	55

Chapter 1

Introduction

This is a line in introduction. This is the introduction to the thesis.

Chapter 2

Quantum Field Theory and The Standard Model

2.1 Quantum Field Theory

2.2 The Standard Model of particle physics

2.2.1 The particle content

Chapter 3

Supersymmetry

3.0.1 Phenomenology of Higgsino production

Chapter 4

Multivariate Statistics

4.1 Decision Trees

Chapter 5

Experimental setup

One of the most useful methods to study the subatomic world of particle physics is by using particle accelerators. In such machines, particles are accelerated to very high speeds and energies, and smashed into each other. The resulted particles are then studied by measuring them in a detector. At the time of writing this thesis, the largest currently active accelerator is the Large Hadron Collider (LHC) near Geneva, Switzerland, operated by the European Organization for Nuclear Research (CERN). For the analysis presented in this thesis, data from the Compact Muon Solenoid (CMS) experiment has been analyzed. In this chapter, the LHC is described in 5.1, while the CMS experiment is described in 5.2.

5.1 The Large Hadron Collider

5.2 The Compact Muon Solenoid experiment

5.3 Simulation of events

Chapter 6

Object reconstruction and identification of particles and jets

6.1 Track reconstruction

This is the track reconstruction page.

6.2 Electrons

6.3 Muons

Chapter 7

Search for compressed Higgsinos with soft lepton tracks

7.1 Motivation

7.2 Signal models

The signal models considered in this analysis are based on **FiXme Note: fill in signal model stuff.**

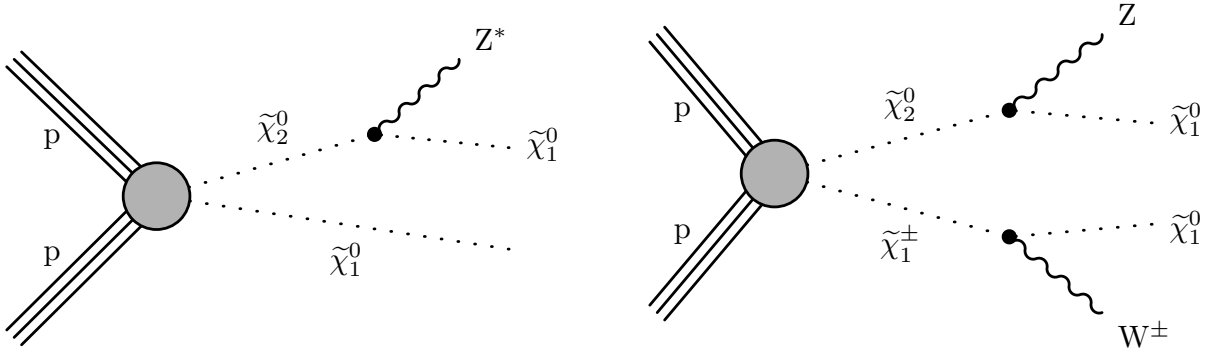


Figure 7.1: Production and decay of electroweakinos in the higgsino simplified model through $\tilde{\chi}_2^0 \tilde{\chi}_1^0$ (left) and $\tilde{\chi}_2^0 \tilde{\chi}_1^\pm$ (right).

7.3 Previous searches

7.4 Search strategy

7.4.1 Exclusive track category

7.5 Signal signature and base selection

To build an effective analysis strategy, the signal kinematics must be studied and exploited. The electroweakino production in question exhibit unique features which can be used in order to discriminate between the signal and the Standard Model (SM) background. It is important to explore these signal distributions in order to define a preselection, or a base cut, that will serve the purpose of retaining as much signal as possible while rejecting as much background. All of the following distributions were plotted by weighting the simulation to Run II luminosity of $\mathcal{L} = 135 \text{ fb}^{-1}$ and requiring at least one jet in the event with $p_T \geq 30 \text{ GeV}$ and $|\eta| < 2.4$. Further selection might apply and will be listed in each section in that case.

7.5.1 Missing Transverse Energy

One property that essentially all Dark Matter (DM) searches have in common is the presence of a DM candidate in the production. The exact identity and properties of said particle (or particles in the case multiple DM candidates) vary, but they do share a lot in common. The DM candidate in our Supersymmetry (SUSY) search is the neutralino, which is a type of DM candidate referred to as a Weakly Interacting Massive Particle (WIMP). A WIMP, broadly speaking, is a new elementary particle which interacts via gravity and any other force (or forces), potentially not part of the SM itself, which is as weak as or weaker than the weak nuclear force, but also non-vanishing in its strength. That essentially means that such candidate is neutral, and therefore not interacting via the electromagnetic force. A neutral particle that interacts neither electromagnetically nor via the strong force (i.e. colorless) will escape detection and will leave traces in the form of a transverse momentum imbalance, which we refer to as E_T^{miss} (Missing Transverse Energy or Missing Transverse Momentum). Our signal contains two DM candidates in the production, which are the Lightest SUSY Particles (LSPs), the neutralinos $\tilde{\chi}_1^0$. We therefore expect the signal to contain considerable magnitude of E_T^{miss} . As described in 7.7.4, **Fixme Note: make sure we described both met and mht** we are more interesting in H_T^{miss} , which is highly correlated with E_T^{miss} , due to our definition of lepton isolation and its use in the background estimation methods. Nonetheless, we will look at both E_T^{miss} and H_T^{miss} observables. **Fixme Note: make sure we define the different deltaM somewhere**

As we expect, E_T^{miss} and H_T^{miss} are hardly affected by the different choices for Δm , while the higgsino parameter μ affect the distributions above all through its lower production cross section for higher higgsino parameter μ . As discuss at 7.8, the region of interest lie at $H_T^{\text{miss}} \geq 220$ for triggering purposes. Even though this is quite a harsh and inefficient cut, one must look also at the SM background at the regions of $H_T^{\text{miss}} < 220$ and $H_T^{\text{miss}} \geq 220$ to conclude that most of the sensitivity comes from the $H_T^{\text{miss}} \geq 220$ region, since the production of real H_T^{miss} (or E_T^{miss}) result from the production of neutrinos in the event, and these are much less common than Quantum Chromodynamics (QCD) events which swarm the $H_T^{\text{miss}} < 220$ region. Therefore, cutting at $H_T^{\text{miss}} \geq 220$ might be inefficient, but results in high sensitivity.

7.5.2 Jets and hardronic activity

Since the neutralinos $\tilde{\chi}_1^0$ escaping the detector are the contributors to the H_T^{miss} and in doing so the drivers of the sensitivity in high H_T^{miss} region, we want them to be as boosted as possible, i.e., with the highest transverse momentum p_T as possible. A widely used approach is to require **Fixme Note: add citation** an Initial State Radiation (ISR) jet in the event. An ISR jet is formed when one of the incoming protons emit radiation (such as a photon or a gluon) before the interaction **Fixme Note: add citation and maybe reference to other section**. If a

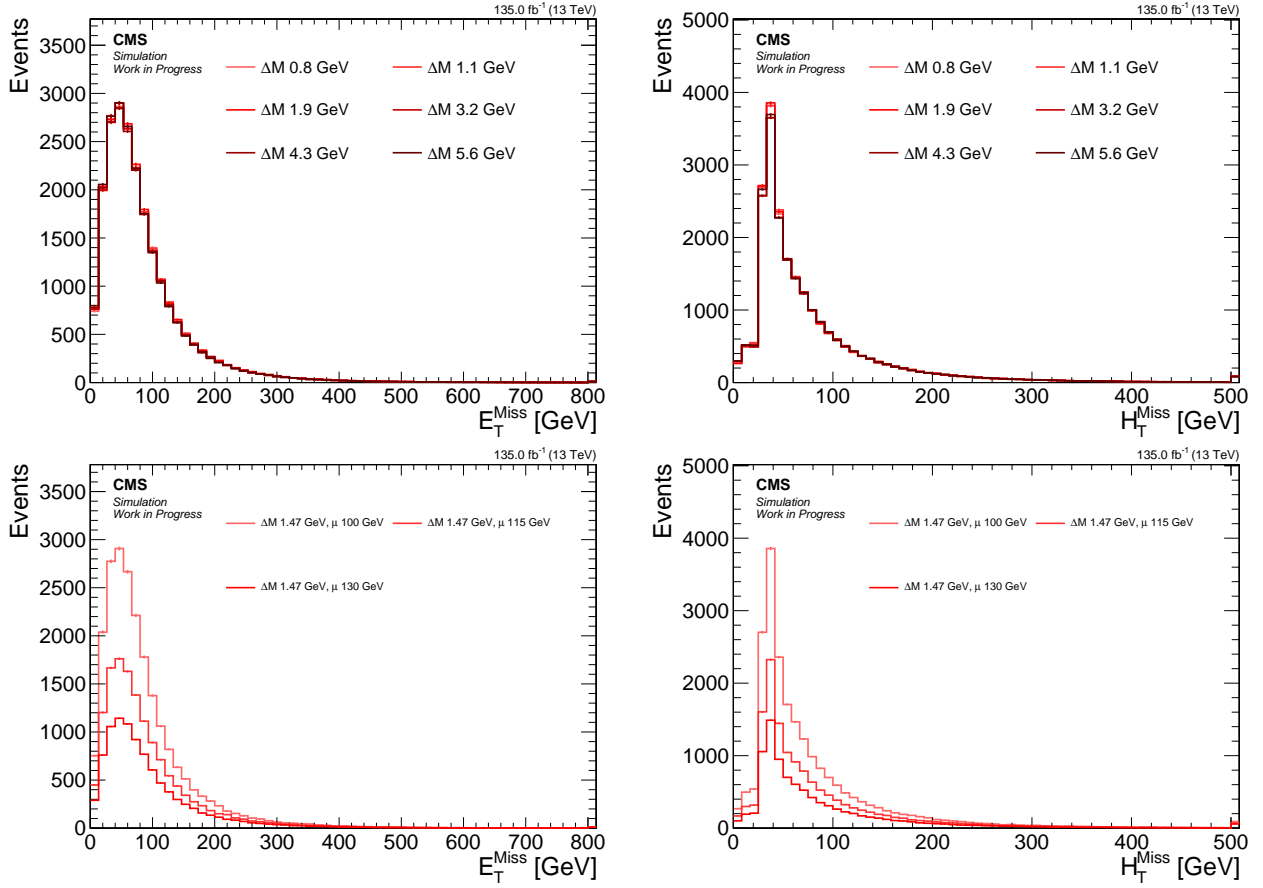


Figure 7.2: Signal distributions for E_T^{miss} (left) and H_T^{miss} (right) comparing various Δm with a fixed higgsino parameter $\mu = 100$ GeV (upper), and comparing various higgsino parameters μ with fixed $\Delta m = 1.47$ GeV (lower).

jet with high enough p_T is emitted, the rest of the interaction is recoiled against this jet and boosting it in the other direction. This way, the boosted neutralinos $\tilde{\chi}_1^0$ will result in higher H_T^{miss} . As described in **FiXme Note: ref**, we require the jets to have $p_T \geq 30$ GeV and be located within the tracker acceptance ($|\eta| < 2.4$). We require at least one such jet in the event.

Our signal signature does not include a b-jet, i.e., a jet resulting from a bottom quark hadronization (either resulting from a top quark or not). We therefore seek to exploit this knowledge by vetoing b-tagged jets in the event. As described in **FiXme Note: add ref** we are using DEEPCSV flavor tagging discriminant with a medium working point. As can be seen in these distributions, most of the signal lie in the 0 bin, and we will therefore veto any b-tagged jet, which retains most of the signal, but rejects a lot of SM background, such as arising from $t\bar{t}$ events.

Since we are requiring an ISR jet in the event, we expect the E_T^{miss} and the H_T^{miss} to point in the opposite direction of the jet, or at least in an angle close to π . Events with multiple jets in the SM background such as arising from QCD will not exhibit such a feature. In order to reduce QCD background, we require $\min \Delta\phi(H_T^{\text{miss}}, \text{jets}) > 0.4$.

7.5.3 Base selection

We recap the section by summarizing the base selection of our analysis. This base selection, or preselection as we might use call it interchangeably, is applied to all analysis categories.

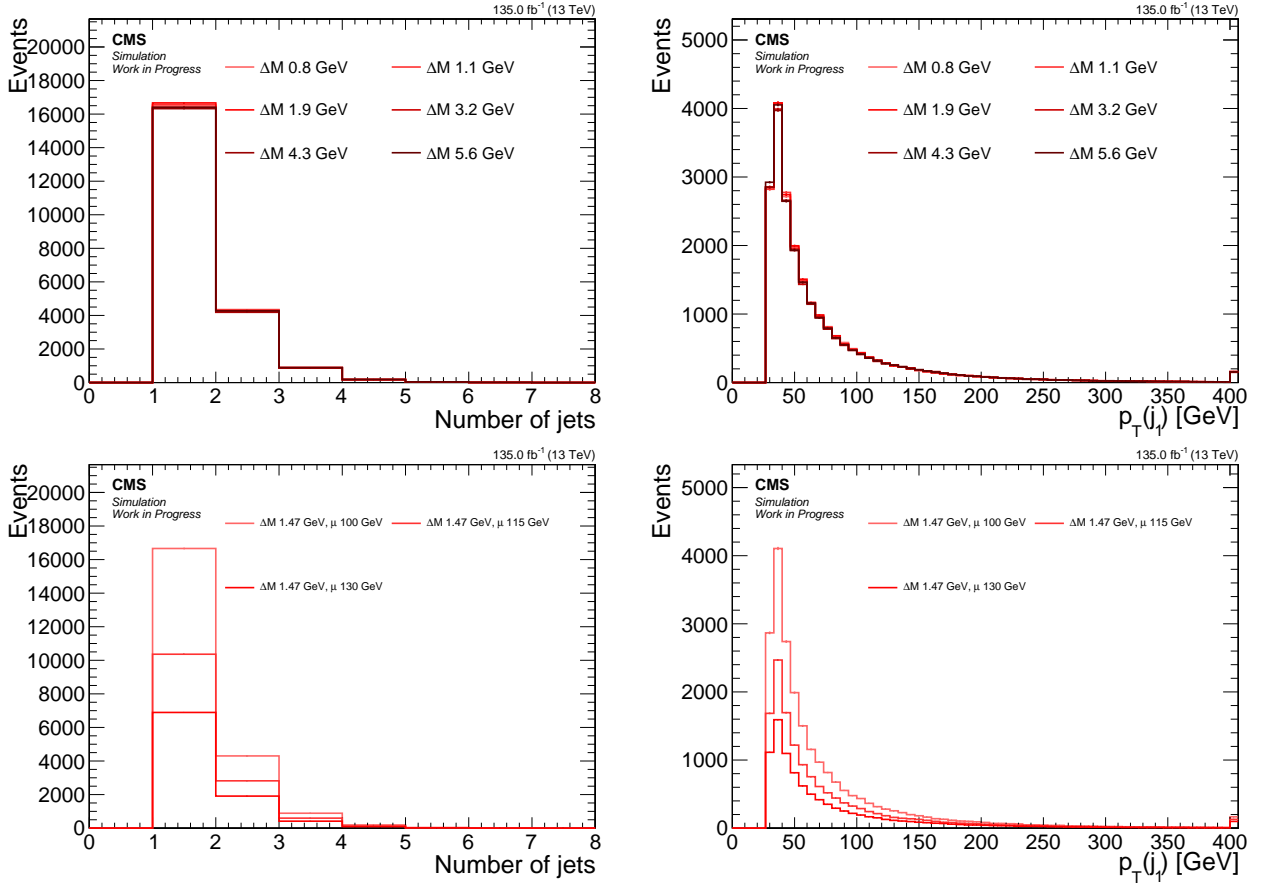


Figure 7.3: Signal distributions for *number of jets* (left) and *leading jet p_T* (right) comparing various Δm with a fixed higgsino parameter $\mu = 100$ GeV (upper), and comparing various higgsino parameters μ with fixed $\Delta m = 1.47$ GeV (lower).

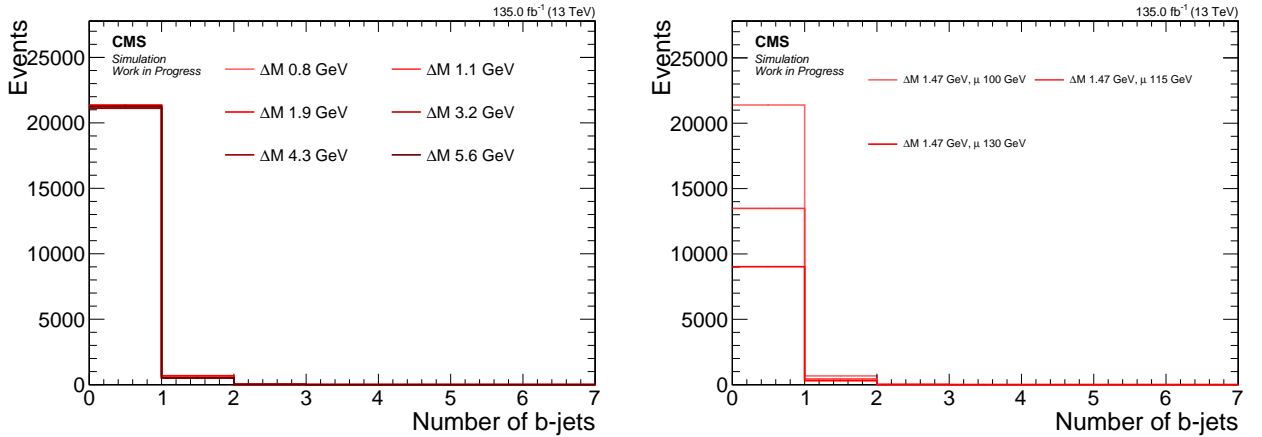


Figure 7.4: Signal distributions for *number of b -tagged jets* comparing various Δm with a fixed higgsino parameter $\mu = 100$ GeV (left), and comparing various higgsino parameters μ with fixed $\Delta m = 1.47$ GeV (right).

7.5.4 Dilepton kinematics

Thus far we have looked at kinematic distributions ignoring the leptons in event. However, the most distinct features of the signal lie in the dilepton system. To fully understand the unique phase space of the dilepton system, we first look at generator level distributions and then look at what effects does reconstruction have on those observables. In addition, since the most sensitive category is the dimuon category due to its much lower threshold on the

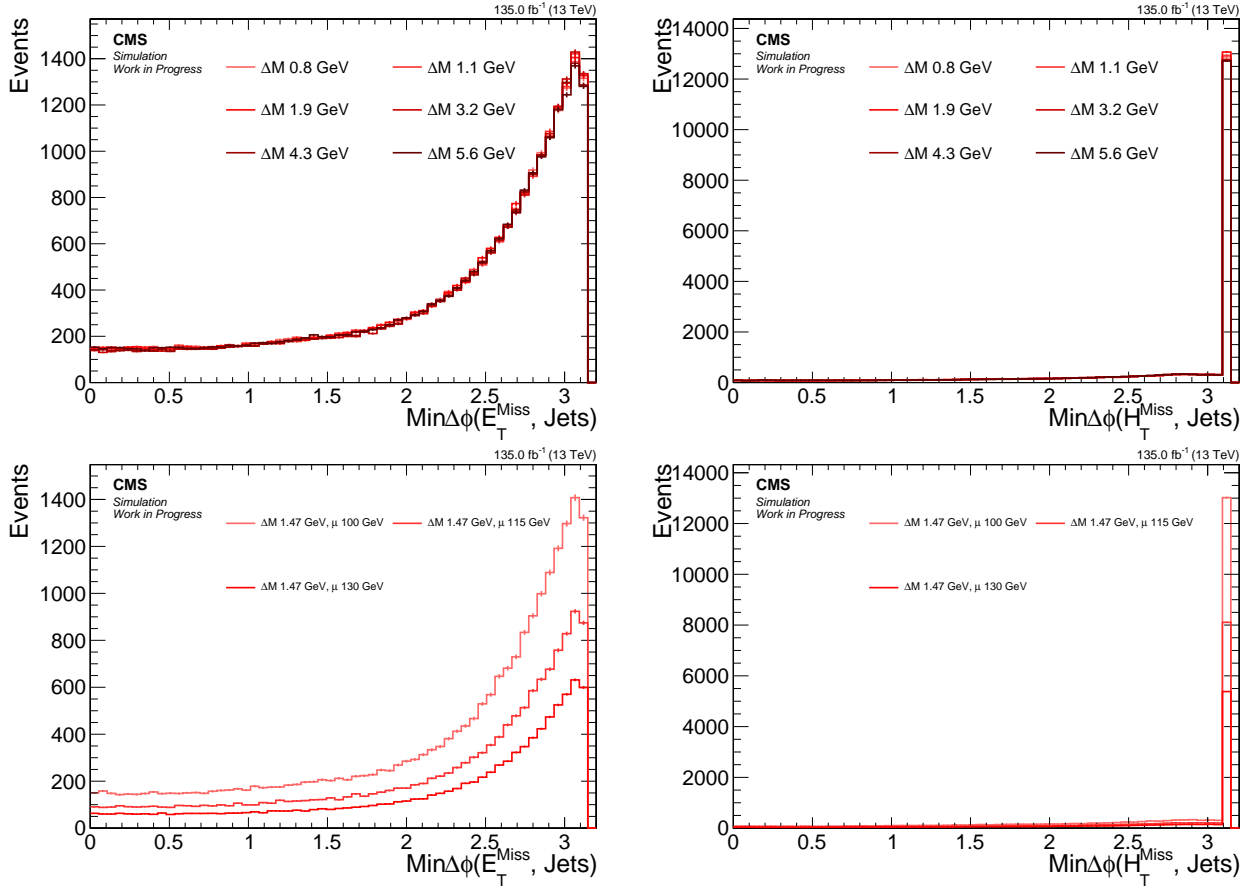


Figure 7.5: Signal distributions for $\min \Delta\phi(E_T^{\text{miss}}, \text{jets})$ (left) and $\min \Delta\phi(H_T^{\text{miss}}, \text{jets})$ (right) comparing various Δm with a fixed higgsino parameter $\mu = 100$ GeV (upper), and comparing various higgsino parameters μ with fixed $\Delta m = 1.47$ GeV (lower).

Table 7.1: Base selection applied to all analysis categories

Variable	Value
H_T^{miss} [GeV]	≥ 220
$N_{\text{jets}} (p_T \geq 30 \text{ GeV and } \eta < 2.4)$	≥ 1
$N_{\text{b-jets}} (p_T \geq 30 \text{ GeV and } \eta < 2.4)$	0
$\min \Delta\phi(H_T^{\text{miss}}, \text{jets})$	> 0.4

transverse momentum, these events are shown in the following sections, leaving the events with two electrons to the appendix **FiXme Note: ref.**

Since the kinematics changes dramatically as a function of Δm , but changes almost only in overall normalization due to the production cross section as a function of the higgsino parameter μ , in the following sections, we set the higgsino parameter to $\mu = 100$ GeV and vary the Δm .

Lepton η and transverse momentum p_T

The transverse momentum p_T distribution of the muons and our access to a subset of its full range, have dramatic effect on the signal acceptance and the sensitivity. The muon reconstruction process and details are discussed in **FiXme Note: ref.** The selection we apply to the muons in this analysis is described in 7.7.2 and will be referred to here as *analysis selection*. In this section we would like to consider specifically the importance of the p_T on the signal and its dilepton kinematic distributions.

We begin by having a look at the generator level distribution of p_T , or in other words, the so-called *truth* distributions, which do not exhibit any detector or reconstruction features, and compare to the reconstructed distribution.

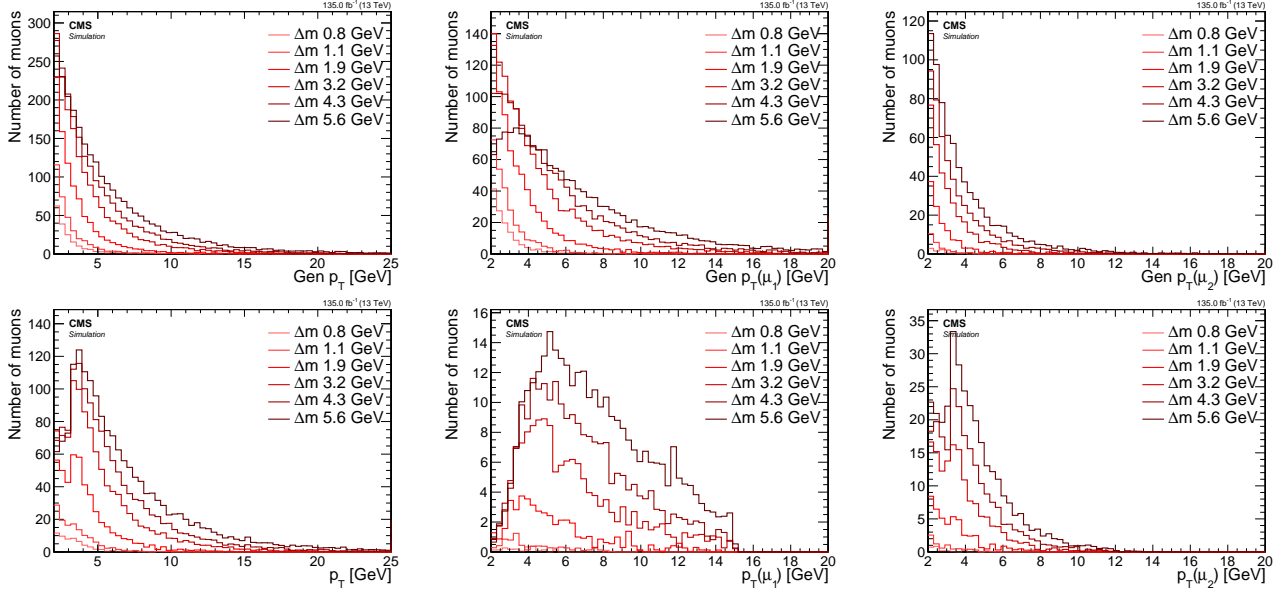


Figure 7.6: Signal p_T distributions for inclusive (left), leading muon μ_1 (middle), subleading muon μ_2 (right) at generator level (top) and reconstruction level passing analysis selection (bottom).

By comparing the generator level to the reconstruction level of the inclusive p_T distribution, we see that a reshaping occurs at around 3 GeV. A significant portion of the generated muons with $p_T < 3$ GeV are being lost in reconstruction. The reconstructed subleading p_T distribution has a camel shape whereby the efficiency drops below p_T of 3 GeV and only partially regained at $p_T < 3$ GeV. This is a detector effect and can be seen more clearly when we split the p_T distribution into a barrel ($|\eta| < 1.2$) and endcaps ($|\eta| \geq 1.2$) portions.

The picture becomes much clearer in regards to the reconstruction efficiency as a function of p_T . When comparing the generator level distribution of the barrel muons on the top left with its constructed counterpart on the bottom left, we see that the barrel is almost completely unable to reconstruct muons with $p_T < 3$ GeV, while the endcaps, shown on the left, are able to do so. As we will see in the $m_{\ell\ell}$ and ΔR upcoming sections (7.5.4 and 7.5.4), since those distribution have an important relationship, that has consequences in regards to reshaping kinematic distributions, as well as signal acceptance in general. Since the low region of $2 \leq p_T \leq 3.5$ GeV is crucial in giving us access to low Δm signal points, it is achieved, as can be seen here, mainly with the help of the muon chamber endcaps.

Since the barrel and endcaps are separated by different regions of η , $|\eta| < 1.2$ for barrel and $|\eta| \geq 1.2$ for endcaps, it worth taking a look at the η distributions of the muons as well.

Our muons analysis selection picks only muons in the tracker range of $|\eta| < 2.4$ which is the reason why the reconstruction plots on the bottom do not have muons with $|\eta| > 2.4$. We see that the main effect going from the inclusive $|\eta|$ in generator level to the reconstructed counterpart, is the flattening of the distribution due to the loss of muons with $|\eta| < 1.2$ in the barrel for muons with $p_T < 3$ GeV.

With the understanding of the reconstruction effects on the p_T and η distributions of the muons, we are equipped to look further into other kinematic variables of the dilepton system.

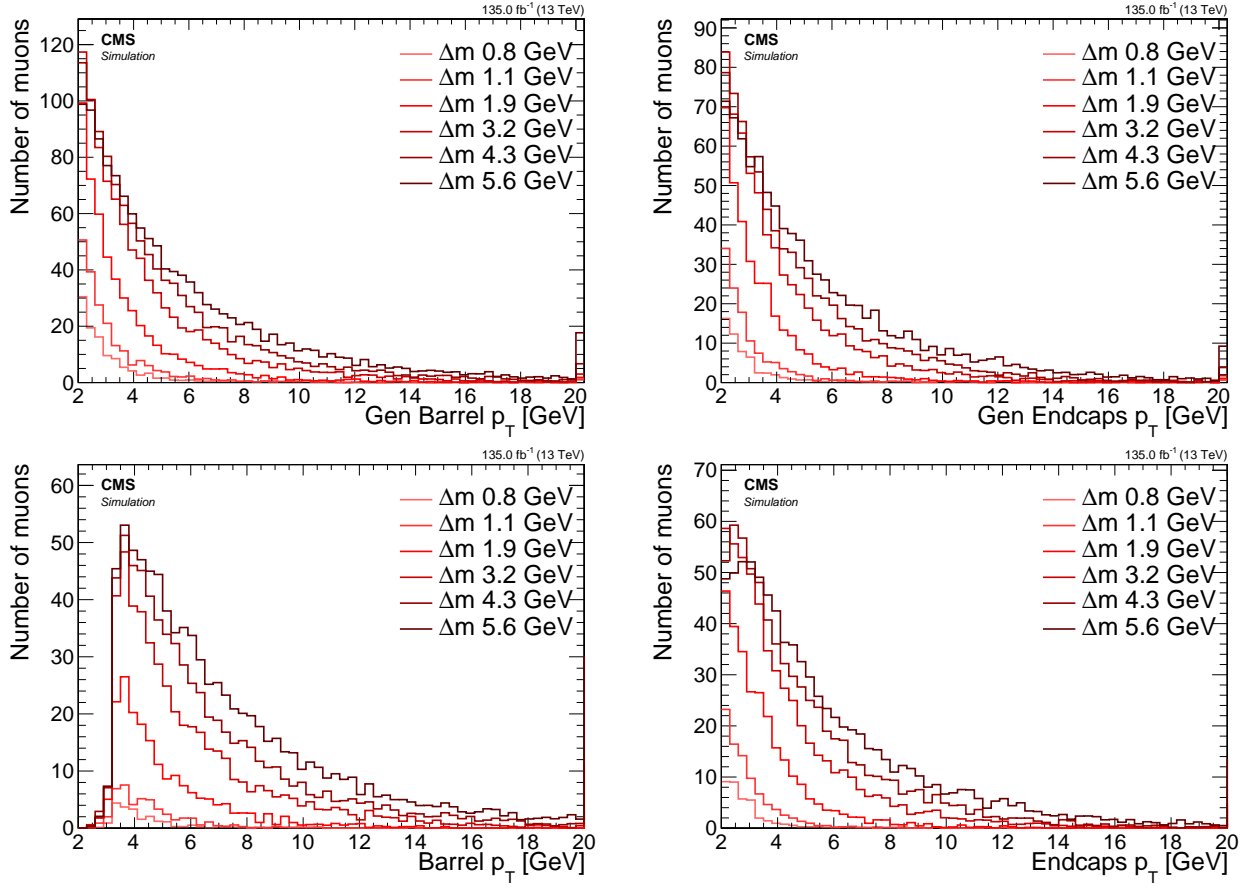


Figure 7.7: Signal inclusive p_T distributions for barrel $|\eta| < 1.2$ (left) and endcaps $|\eta| \geq 1.2$ (right) at generator level (top) and reconstruction level passing analysis selection (bottom).

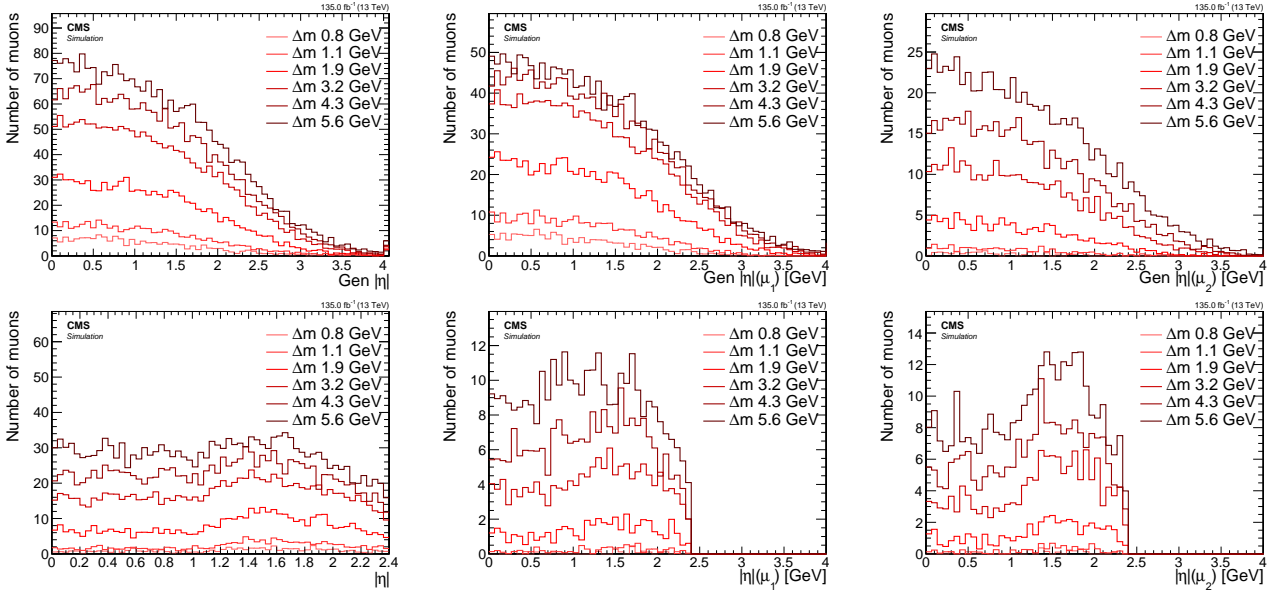


Figure 7.8: Signal $|\eta|$ distributions for inclusive (left), leading muon μ_1 (middle), subleading muon μ_2 (right) at generator level (top) and reconstruction level passing analysis selection (bottom).

Invariant mass $m_{\ell\ell}$

The invariant mass of the two leptons that result from the decay of the $\tilde{\chi}_2^0$ has a unique shape due to the limited allowed phase space of the leptons as part of the 3-body decay. Since the $\tilde{\chi}_2^0$

decays into $\tilde{\chi}_1^0$ and $\ell^+\ell^-$ through a Z^* , the allowed phase space of the dilepton pair is restricted to the mass difference between $\tilde{\chi}_2^0$ and $\tilde{\chi}_1^0$, i.e., Δm . We therefore expect the $m_{\ell\ell}$ distribution to have an edge at Δm .

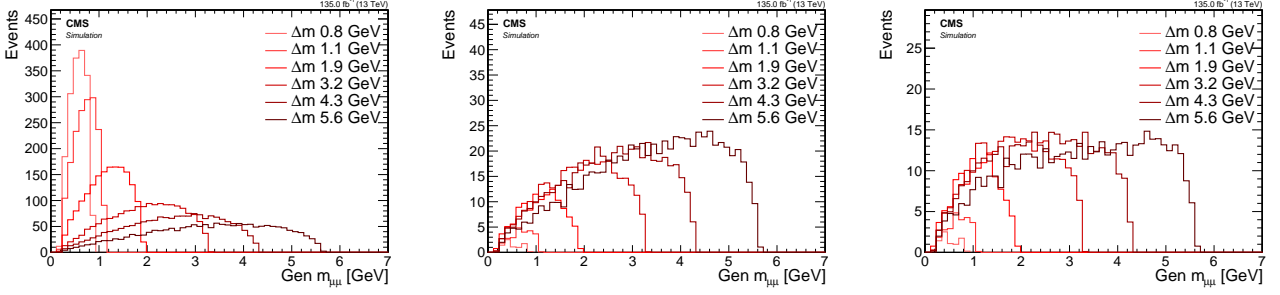


Figure 7.9: Signal generator level $m_{\ell\ell}$ distributions with no cuts (left), with $p_T(\mu_i) > 2 \text{ GeV}$, $i = 1, 2$ (middle) and with SOS orthogonality condition $p_T(\mu_i) > 2 \text{ GeV}$, $p_T(\mu_2) \leq 3.5 \text{ GeV}$ or $\Delta R \leq 0.3$ (right).

We see the original invariant mass of the muons $m_{\mu\mu}$ on the left. For each signal point, the edge of the $m_{\mu\mu}$ distribution is right at the corresponding Δm . However, once we cut on the muons p_T and require $p_T \geq 2 \text{ GeV}$, the shape shifts, and the efficiency in the lower Δm drops dramatically, as can be seen from the middle plot. Lastly, the effect of orthogonalizing phase space to the SOS analysis can be seen on the right most plot. The effect is strongest in high Δm and quite subtle in low Δm .

To understand the reshaping that happens to the $m_{\mu\mu}$ shape, we look at the relationship between the p_T of the muons (leading muon denoted μ_1 while subleading muon is denoted μ_2) and the invariant mass one a signal with low Δm of 1.13 GeV and one with high Δm of 5.63 GeV.

We have established earlier that the invariant mass distribution has an edge at the Δm and one can read the value of Δm from these plots. Another interesting feature to notice in these plots is that there is also a lower edge in the Δm distribution at around $\sim 0.2 \text{ GeV}$ and that is of course due to each muon having a mass of around $\sim 0.1 \text{ GeV}$. We can clearly see now that by cutting on both muons at $p_T \geq 2 \text{ GeV}$, we are losing a lot of the signal. This effect, in fact, becomes quite substantial for the low $\Delta m = 1.13 \text{ GeV}$ (top row). We quantify this effect by making a cutflow table where each row represents a cut, and its efficiency is calculated by dividing the number of events passing the cut by the number of events in the line before it. The first line is our baseline of all dimuon events with at least one jet with $p_T \geq 30 \text{ GeV}$ and $|\eta| < 2.4$ and has an efficiency of 1 by definition. The event number is weighted to Run II luminosity of $\mathcal{L} = 135 \text{ fb}^{-1}$.

Table 7.2: Generator level efficiency on muons selections

Cut	Number of events		Efficiency	
	$\Delta m = 1.13 \text{ GeV}$	$\Delta m = 5.63 \text{ GeV}$	$\Delta m = 1.13 \text{ GeV}$	$\Delta m = 5.63 \text{ GeV}$
Baseline	1710.7	1743.9	1	1
$p_T \geq 2 \text{ GeV}$	24.7	724.9	0.015	0.41
SOS orthogonality	24.7	490.6	1	0.68

We observe that for the low Δm of 1.13 GeV the cut of $p_T \geq 2 \text{ GeV}$ is really hurting the acceptance of the signal with only 1.5% of signal remaining. In contrast, the orthogonality condition of requiring $p_T(\mu_2) \leq 3.5 \text{ GeV}$ or $\Delta R(\ell\ell) \leq 0.3$ is not effecting it any further. The picture is different for the high Δm of 5.63 GeV where the p_T cut is cutting away more than half of the signal and the SOS orthogonality an additional two thirds.

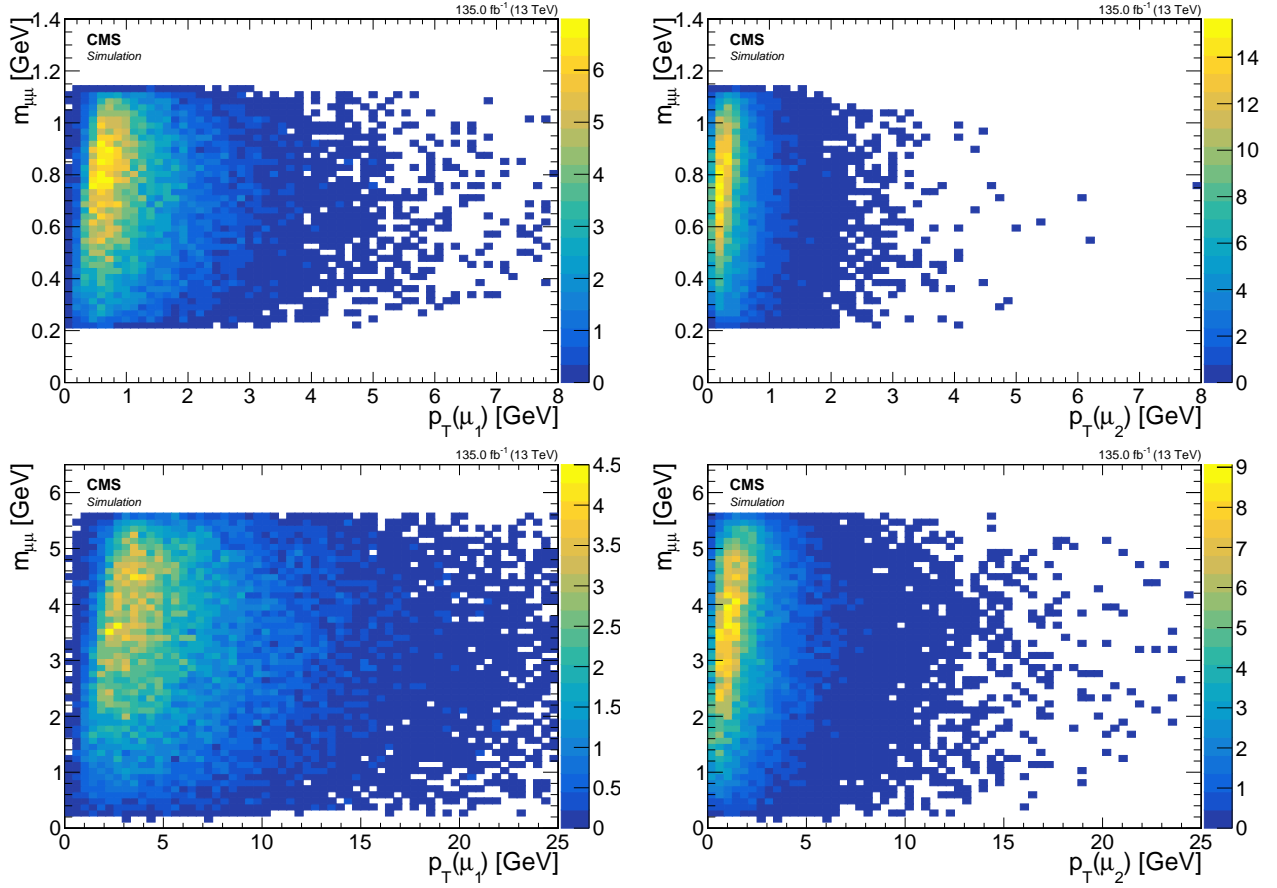


Figure 7.10: Signal $m_{\mu\mu}$ vs. p_T for leading lepton μ_1 (left) and subleading lepton μ_2 (right) for $\Delta m = 1.13$ GeV (top) and $\Delta m = 5.63$ GeV (bottom).

Since we have just established that due to the relationship between p_T and $m_{\ell\ell}$, the p_T distribution directly effects $m_{\ell\ell}$, we should also have a look at how to reconstruction effects discussed at 7.5.4 might effect the $m_{\mu\mu}$ distribution as well.

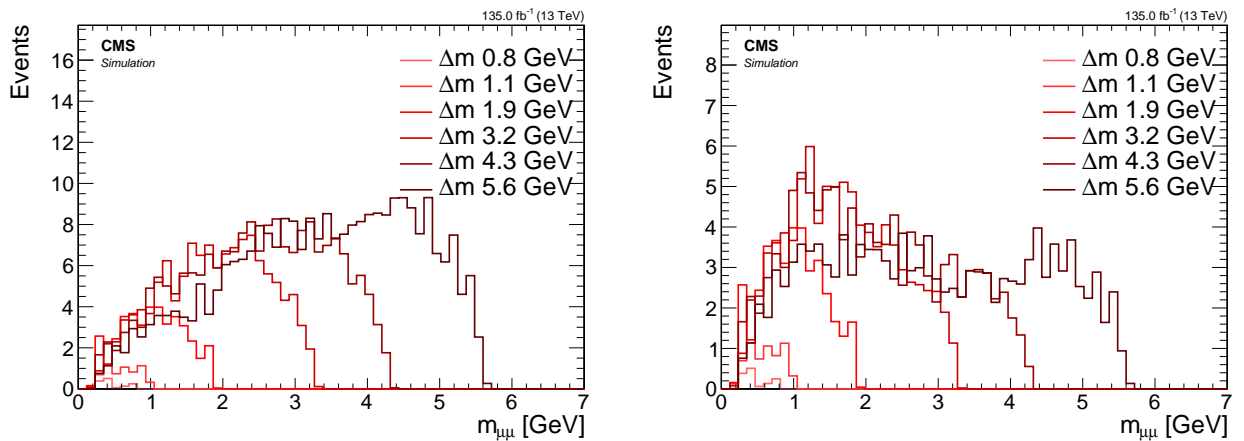


Figure 7.11: Signal reconstructed $m_{\mu\mu}$ with basic analysis selection (left) and additional SOS orthogonality condition (right).

It's interesting to compare these distributions to the two right ones in the generator level version at 7.9. We see that not only less events survive the reconstruction, but also that some Δm model points peak between 1 GeV to 2 GeV with SOS orthogonality condition applied. The reconstruction and selection efficiency is discussed in more details in **FiXme Note: ref.**

Lepton separation ΔR

The lepton separation is defined by $\Delta R = \sqrt{(\Delta\eta)^2 + (\Delta\phi)^2}$ where η is the pseudorapidity and ϕ is the azimuthal angle measured in radians. ΔR plays a major role in this analysis since the leptons tend to be produced in proximity to each other and thus to defy standard definitions of isolation. Special care is taken to ensure that the collimated nature of the leptons can still be used to distinguish the otherwise isolated leptons in the signal from the non-isolated leptons in the SM background. An additional point of interest is with respect to previous SOS analysis **FiXme Note:** cite that had a requirement of $\Delta R(\ell\ell) > 0.3$ which we attempt to revert here for orthogonality purposes.

In similar fashion to the invariant mass in 7.5.4, we look at distributions of ΔR for various choices of Δm with different cuts applied, and observe their effect.

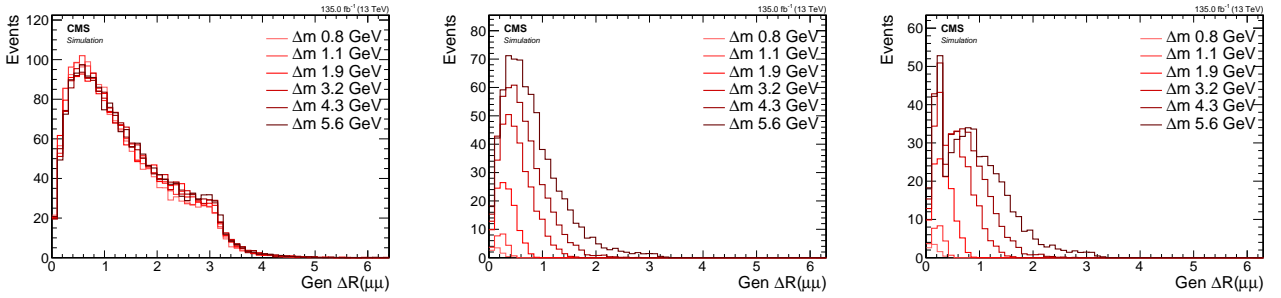


Figure 7.12: Signal generator level ΔR distributions with no cuts (left), with $p_T(\mu_i) > 2 \text{ GeV}$, $i = 1, 2$ (middle) and with SOS orthogonality condition $p_T(\mu_i) > 2 \text{ GeV}$, $p_T(\mu_2) \leq 3.5 \text{ GeV}$ or $\Delta R \leq 0.3$ (right).

As can be seen on the left plot, roughly the same amount of events are produced for all Δm model points, but when applying a cut of $p_T(\mu) > 2 \text{ GeV}$, a hierarchy of Δm points forms, with less events as Δm becomes smaller (middle plot). The spike on the right plot is due to the SOS orthogonality condition which requires $\Delta R(\ell\ell) \leq 0.3$ as one of two conditions in an or statement. To understand the shaping and hierarchy formation due to the p_T cut, we repeat the trick from the $m_{\mu\mu}$ in 7.5.4 and plot the p_T of the muons vs. $\Delta R(\ell\ell)$.

Now the hierarchy can be understood by observing that for $\Delta m = 1.13 \text{ GeV}$, cutting $p_T(\mu_2) \geq 2 \text{ GeV}$ will limit the range of $\Delta R(\mu\mu)$ to less than 0.4 while leaving quite a large range exceeding 3 for the $\Delta m = 5.63 \text{ GeV}$ model point.

We conclude therefore, that even before taking into consideration reconstruction efficiency of the leptons, to gain access and sensitivity to the low Δm model points, we must be able to probe low $\Delta R(\ell\ell)$ values, potentially with values less than 0.3. In the next sections we will need to study reconstructed leptons and define isolation criteria that will enable us to retain signal points with close lepton pairs.

As we have seen for $m_{\mu\mu}$ in 7.5.4, reconstruction has an effect on both the shape and overall count of events. We look here at those effects on the $\Delta R(\mu\mu)$ distributions.

When we compare the reconstructed $\Delta R(\mu\mu)$ distributions 7.14 to the generator level ones at 7.12 we see that the main effect of the reconstruction on the $\Delta R(\mu\mu)$ is the overall normalization due to reconstruction efficiency.

7.5.5 Main drivers of sensitivity

We attempt to draw conclusion from this signal distribution studies in regards to the main drivers to the sensitivity of different model points of this analysis, as well as of future analysis that might attempt to expend on this one. In this section we have not looked at SM background

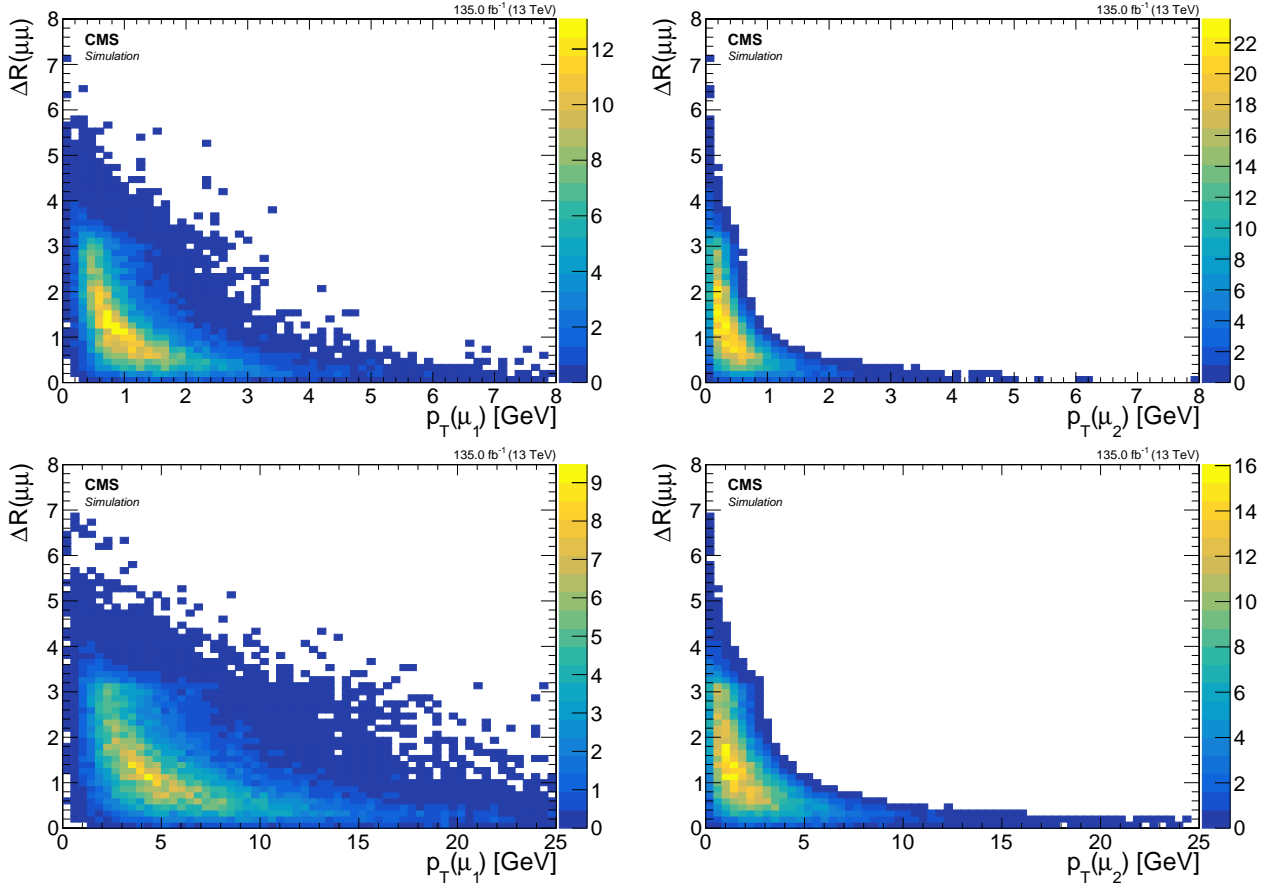


Figure 7.13: Signal $\Delta R(\mu\mu)$ vs. p_T for leading lepton μ_1 (left) and subleading lepton μ_2 (right) for $\Delta m = 1.13$ GeV (top) and $\Delta m = 5.63$ GeV (bottom).

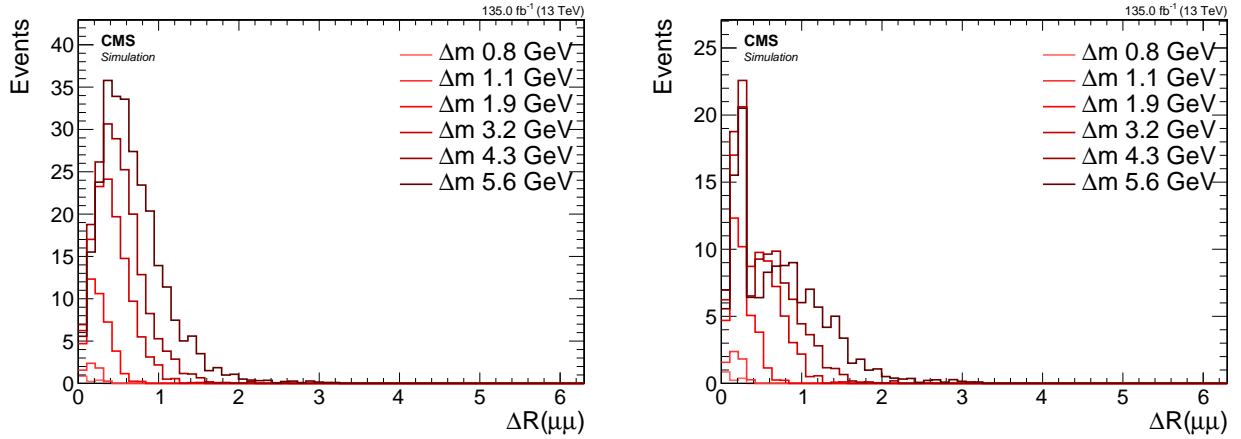


Figure 7.14: Signal reconstructed $\Delta R(\mu\mu)$ with basic analysis selection (left) and additional SOS orthogonality condition (right).

at all. Therefore, it is hard to conclude what effects changing the cuts to E_T^{miss} or other event level observables might have. However, one thing is very clear from examining the dilepton kinematics and that is that to gain access to low Δm model points, one must lower the threshold on of p_T in the selection of the decay leptons and make sure to also be able to probe low ΔR . Another driver of the sensitivity at all Δm model points is the luminosity, since the production cross section drops as a function of the higgsino mass parameter μ .

We will explore in the next sections how we are able to lower the threshold on the muons transverse momentum as well as dealing with collimated leptons that might pose a challenge.

7.6 Simulated samples

7.6.1 Standard Model simulated samples

7.6.2 Signal simulated samples

7.7 Object definition and selection

We have seen in 6 how objects are being reconstructed and identified in our detector. We have also studied the signal signature in 7.5. In this section we devise an object selection in order to obtain as pure as possible sample of objects in regards to our target leptons, while retaining as much signal as possible. As we have seen in 7.4, we are targeting the opposite-charged same-flavor leptons $\ell^+\ell^-$ that result from the $\tilde{\chi}_2^0$ that decays into a $\tilde{\chi}_1^0$ via a Z^* , i.e., $\tilde{\chi}_2^0 \rightarrow \tilde{\chi}_1^0 \ell^+ \ell^-$. In the following section, we choose to present two choices of Δm^0 , namely, $\Delta m^0 = 1.92 \text{ GeV}$ and $\Delta m^0 = 5.63 \text{ GeV}$, i.e., a relatively high Δm^0 , and a low one, but not too low as to still be able to have enough electrons surviving the initial reconstruction p_T threshold of 5 GeV. We also fix the higgsino parameter on $\mu = 100 \text{ GeV}$.

As was the case in 7.5, the base selection for the following section is requiring at least one jet in the event with $p_T \geq 30 \text{ GeV}$ and $|\eta| < 2.4$. No other selections otherwise. However, unlike 7.5, we do not weight our objects to any luminosity, as we are interested in the proportion between object types. We differentiate between two types of leptons, ones that originate from our targeted decay $\tilde{\chi}_2^0 \rightarrow \tilde{\chi}_1^0 \ell^+ \ell^-$, which will be shown in blue, and those that do not, which we refer to as *other*, and are shown in yellow. Leptons that are marked as resulting from the $\tilde{\chi}_2^0 \rightarrow \tilde{\chi}_1^0 \ell^+ \ell^-$ decay, which we will refer to as *signal leptons*, are done so by matching a reconstructed lepton to a generator level lepton, which has been checked to have the $\tilde{\chi}_2^0$ as its parent. Lepton marked as *other*, either has been misreconstructed, misidentified or is a result of hadronisation process in a jet (such as the ISR jet). Our goal here is to select as many blue leptons as possible, while rejecting as many yellow ones as possible. In the following sections, we will refer to *efficiency* as the proportion between the signal leptons passing a selection, divided by the initial number of signal leptons, and to *purity* as the proportion between signal leptons (blue) and the sum of the signal leptons and *other* leptons (yellow). So to rephrase our goal, we are interested in a selection that results in high-efficiency and high-purity. These two quantities can sometimes compete with each other and we have to make compromises.

7.7.1 Electrons

The electrons have an initial reconstruction p_T threshold of 5 GeV. The initial working point choice for reconstructed electron is loose (see 6). The first distribution we look at in regards to the electrons is their spatial separation from the leading jet in the event, $\Delta R(j_1, e)$.

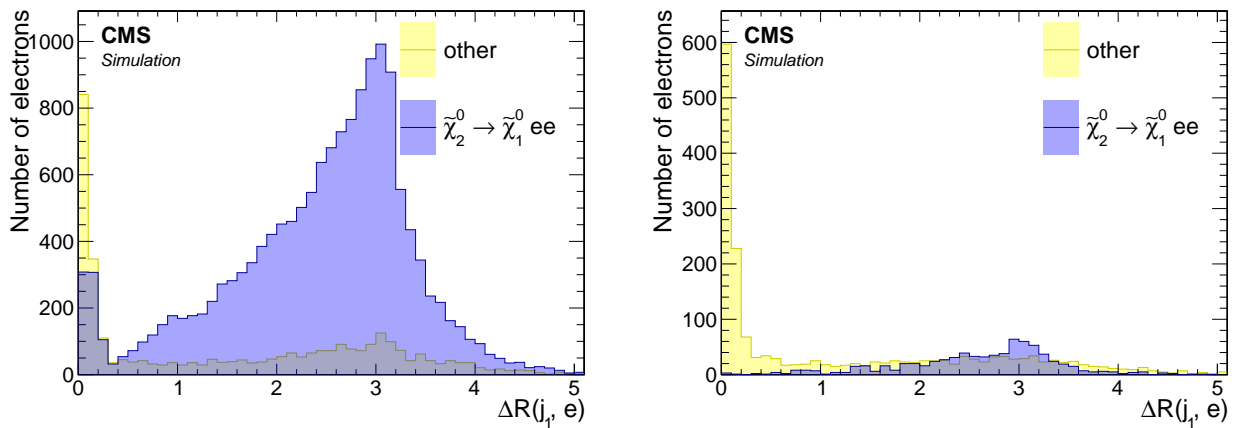


Figure 7.15: Spatial separation between reconstructed electrons with loose ID and the leading jet $\Delta R(j_1, e)$ for $\Delta m = 5.63 \text{ GeV}$ (left) and $\Delta m = 1.92 \text{ GeV}$ (right).

There are two obvious features we can take from these plots. The first we have explored already in 7.5, namely, that probing lower Δm requires access to low p_T leptons, and since we

are limited by a lower threshold of $p_T \geq 5 \text{ GeV}$ on the electrons, that results in lower signal acceptance as can be seen by the difference between the high Δm and the low one. The second interesting feature that we can see, is that our signal electrons are located mainly outside of the leading jet. That is because the leading jet is usually an ISR jet which boosts the $\tilde{\chi}_2^0 \tilde{\chi}_1^0$ system to away from it (back-to-back). We therefore make a cut $\Delta R(j_1, e) > 0.4$.

Next we turn into the p_T distributions. We apply the previous cut of $\Delta R(j_1, e) > 0.4$. As we've already seen in 7.5.4, the p_T distribution depends strongly on Δm . Even though the distributions in 7.5.4 were plotted using generator level muons, the electrons distributions follow the same trend. We therefore need to make a choice about which Δm to favor, i.e., which Δm we want to be more sensitive to, and we choose the lower Δm case. Nonetheless we compare the two choices.

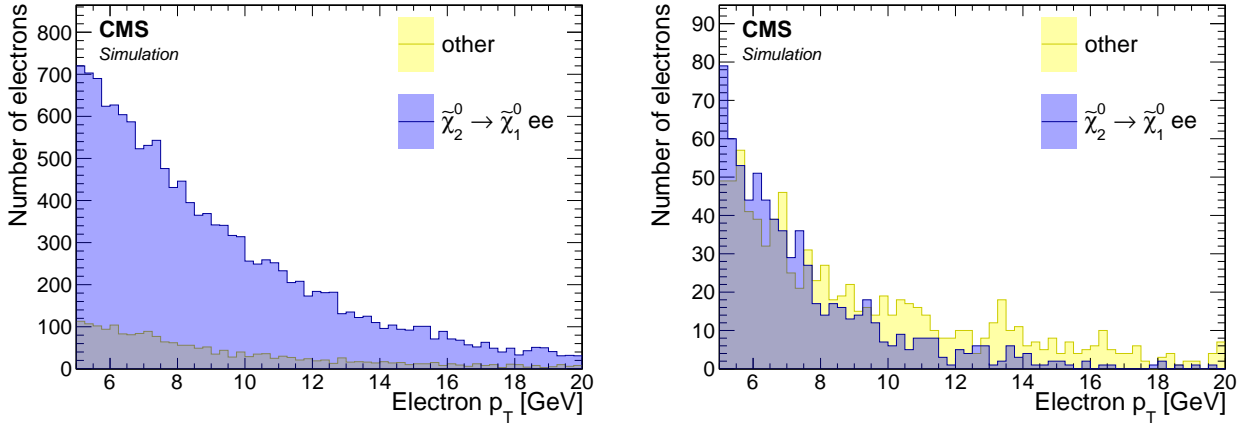


Figure 7.16: p_T distribution of reconstructed electrons with loose ID for $\Delta m = 5.63 \text{ GeV}$ (left) and $\Delta m = 1.92 \text{ GeV}$ (right). Cut of $\Delta R(j_1, e) > 0.4$ applied.

We can see, as expected, that the p_T distribution of the electrons fall more rapidly for the low Δm case. We observe that there are hardly any electrons surviving above 15 GeV , and therefore we choose to make a cut of $p_T < 15 \text{ GeV}$.

It interesting to look at the η distribution after the previous cuts to get a better sense of where most of the non-signal electrons are stil coming from.

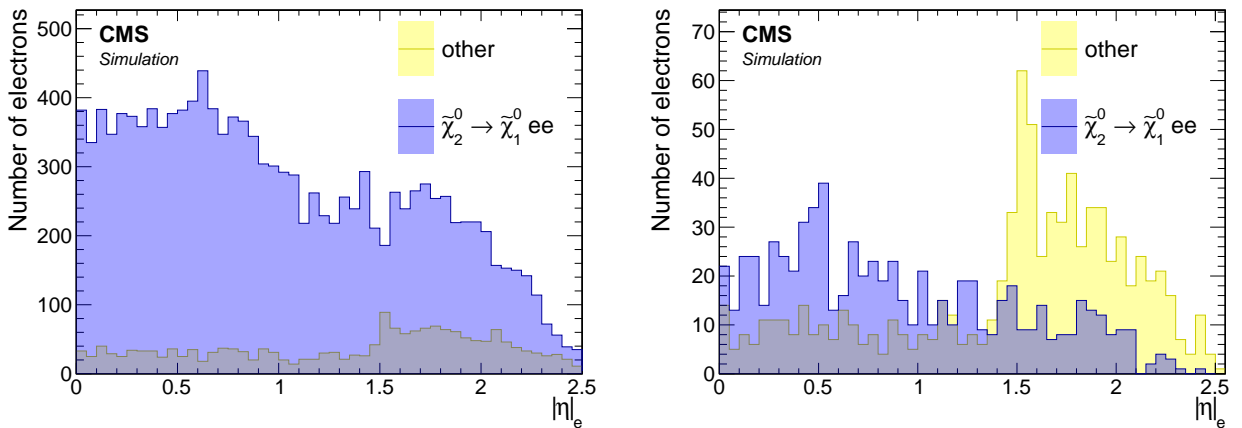


Figure 7.17: $|\eta|$ distribution of reconstructed electrons with loose ID for $\Delta m = 5.63 \text{ GeV}$ (left) and $\Delta m = 1.92 \text{ GeV}$ (right). Cuts of $\Delta R(j_1, e) > 0.4$ and $p_T < 15 \text{ GeV}$ are applied.

In the case of $\Delta m = 1.92 \text{ GeV}$, we can clearly see how worse the endcaps of the Electro-magnetic Calorimeter (ECAL) are performing in comparison with the barrel ($|\eta| < 1.48$). The

transition is clearly visible through a sharp drop in purity at the transition. It is worse for low- p_T electrons than higher- p_T ones.

We would like to see if requiring a tighter working point for the electron-identification is beneficial. The working point used in the previous distributions is loose. We look turn now to check the effects of requiring either a medium working point, or a tight one. We plot two bins labeled *fail* and *pass*, which correspond to whether the electron passes or failed the identification criteria of a medium or tight working points.

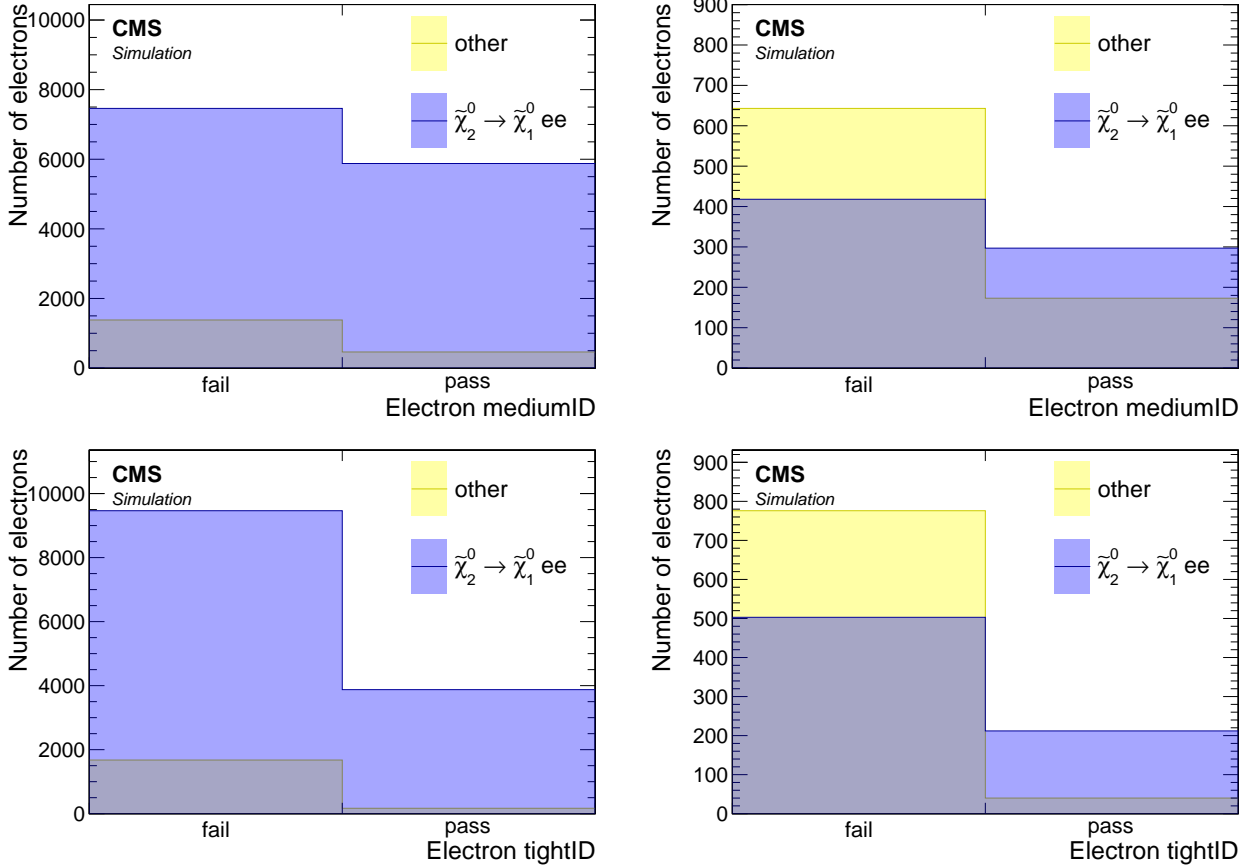


Figure 7.18: Medium (top) and tight (bottom) ID working points distributions of reconstructed electrons for $\Delta m = 5.63$ GeV (left) and $\Delta m = 1.92$ GeV (right). Cuts of $\Delta R(j_1, e) > 0.4$ and $p_T < 15$ GeV are applied.

Selecting a medium or a tight working point is equivalent to choosing the relevant right *pass* bin (top for medium, bottom for tight), and rejecting the electrons on the left *fail* bin. We see that although we reject considerable amount of non-signal electrons in the low Δm case by picking either a medium or tight working points, we also loose quite a lot of signal electrons as well. In other words, these selections are very not efficient and will result in low signal acceptance. We therefore decide to use a loose working point for the electrons. We will see that we can still purify the electron selection by relying on isolation instead. We fully discuss and describe our jet-isolation in 7.7.6, but here for the sake of completeness we look at its effect on the purity of the electrons. We compare our custom jet-isolation to the standard definition of lepton isolation, which does not take into account the possibility that two electrons can be produced close to each other (small ΔR), as is the case in our signal.

We observe that the standard lepton isolation does not perform well in terms of efficiency for both Δm cases. In contrast, the custom jet-isolation is performing very well in terms of signal electron efficiency while successfully rejecting considerable amount of non-signal electrons, resulting in a purer sample of electrons. We therefore conclude that the choice of the custom

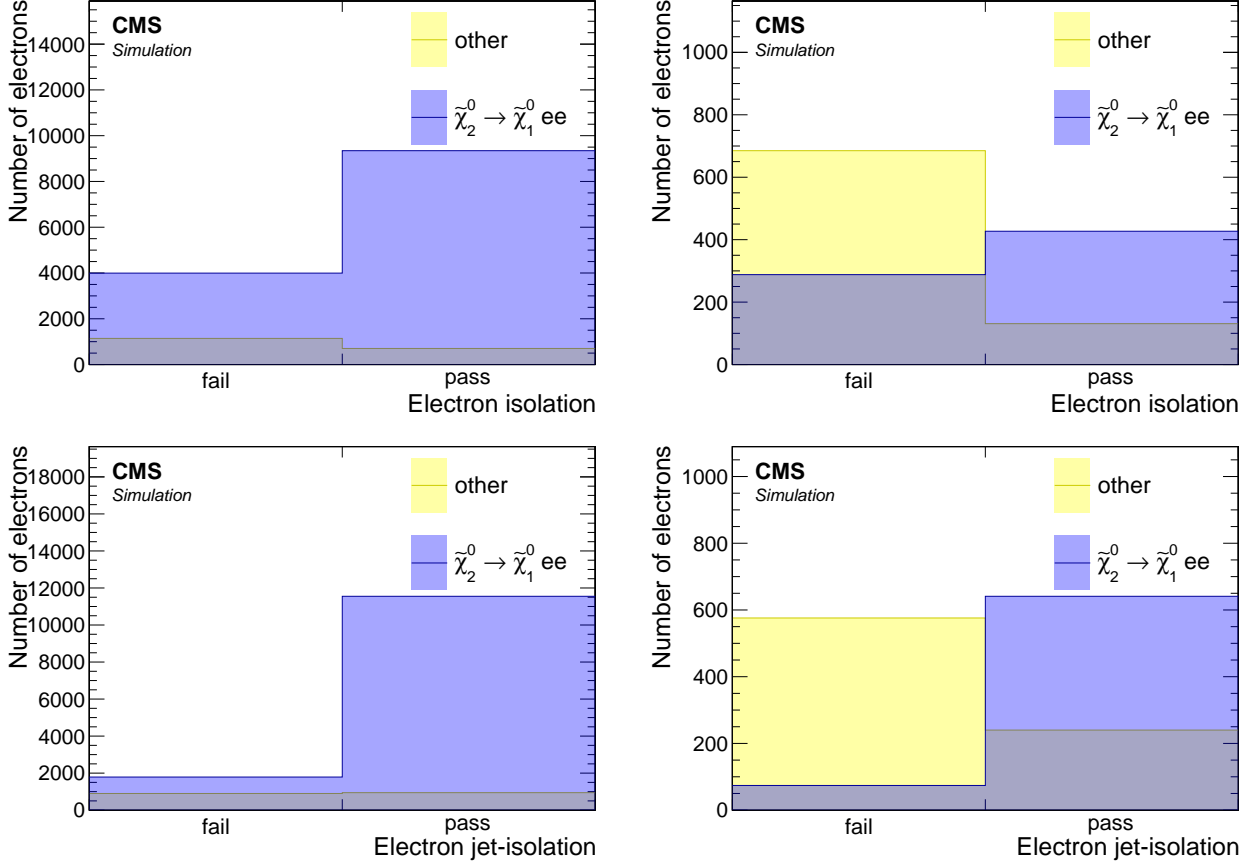


Figure 7.19: Standard isolation (top) and custom jet-isolation (bottom) distributions of reconstructed electrons with loose ID for $\Delta m = 5.63$ GeV (left) and $\Delta m = 1.92$ GeV (right). Cuts of $\Delta R(j_1, e) > 0.4$ and $p_T < 15$ GeV are applied.

jet-isolation is favorable. We can look at how the η distribution is affected by this choice and that will conclude our selection of the electrons.

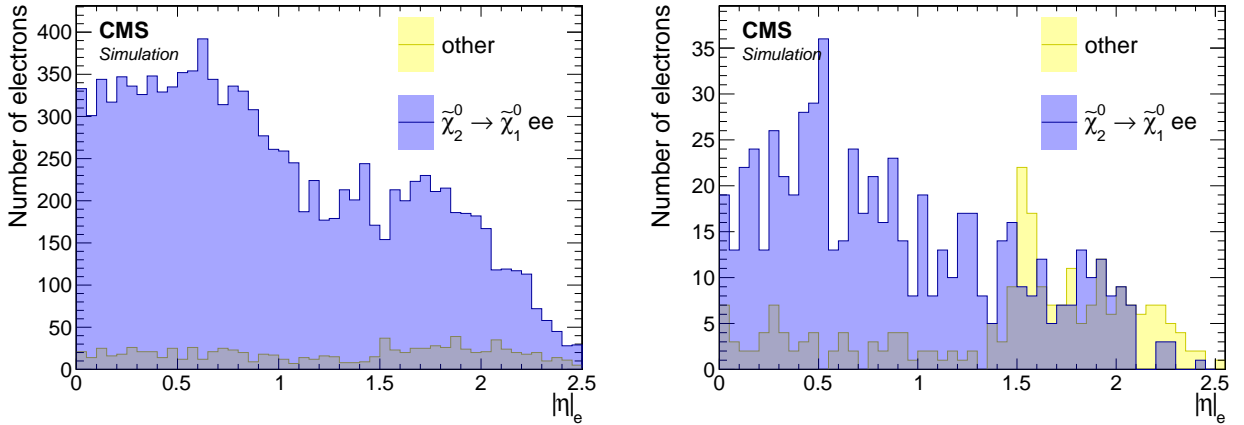


Figure 7.20: $|\eta|$ distribution of reconstructed electrons with loose ID passing jet-isolation for $\Delta m = 5.63$ GeV (left) and $\Delta m = 1.92$ GeV (right). Cuts of $\Delta R(j_1, e) > 0.4$ and $p_T < 15$ GeV are applied.

When we compare distributions 7.20 with 7.17, we can see that our custom jet-isolation has done a good job purifying the electrons selection even further while being efficient in retaining the signal electrons.

We summaries this section with the full selection of the analysis electrons:

- $5 < p_T < 15 \text{ GeV}$
- $|\eta| < 2.5$
- $\Delta R(j_1, e) > 0.4$
- loose ID working point
- pass jet-isolation

7.7.2 Muons

In contrast to the electrons, we do not have an initial reconstruction p_T threshold of 5 GeV. Therefore, we want to explore the possibility of lowering the p_T threshold as much as possible. This has been motivated in section 7.5.4, where we saw that the lower Δm we want to probe, the lower p_T threshold we have to allow. Like in the electron case, the initial working point choice for reconstructed muon is loose (see 6). We follow a similar procedure to the electrons case. The first distribution we look at in regards to the muons is their spatial separation from the leading jet in the event, $\Delta R(j_1, \mu)$. We have seen in 7.7 that the muon endcaps are capable of reconstructing muons with $p_T < 3 \text{ GeV}$ while the barrel cannot. It therefore makes sense to look at a split view of barrel and endcaps for the following distributions.

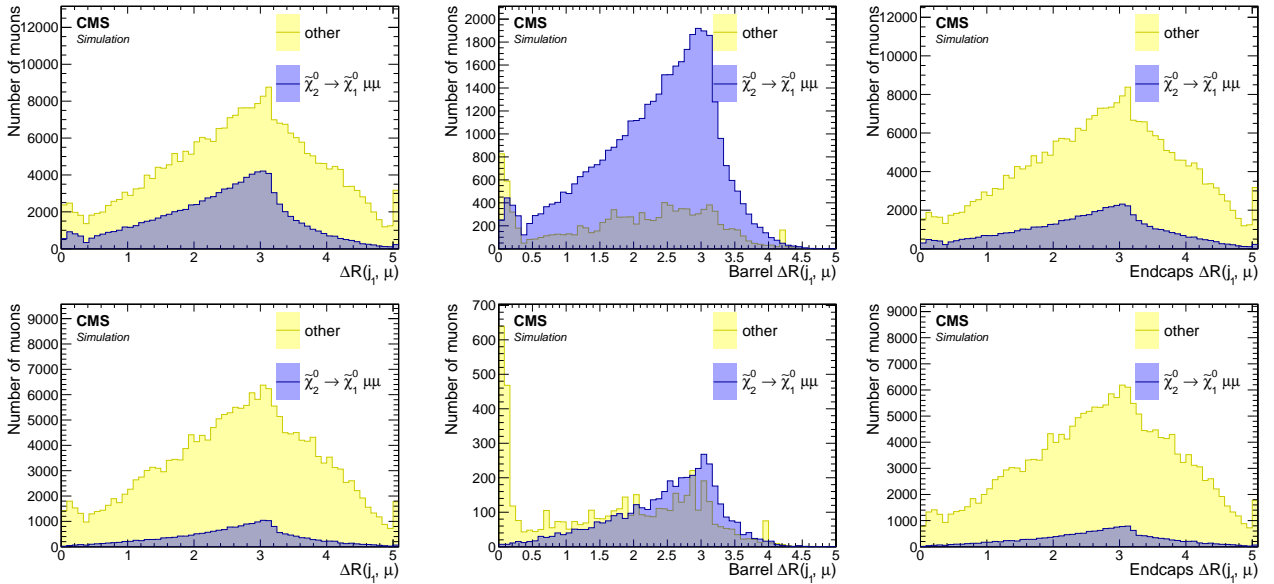


Figure 7.21: Spatial separation between reconstructed muons with loose ID and the leading jet $\Delta R(j_1, \mu)$ for $\Delta m = 5.63 \text{ GeV}$ (top) and $\Delta m = 1.92 \text{ GeV}$ (bottom) in the inclusive case (left), barrel (middle) and endcaps (right).

Since the muons in the endcaps has lower p_T than the muons in the barrel, which is able to reconstruct muons with $p_T > 3 \text{ GeV}$ only, the purity in the endcaps is much lower than the purity in the barrel, and the selection we are constructing here attempts to purify the muons further. Just as in the electrons case, we select muons with $\Delta R(j_1, \mu) > 0.4$, and that selection will apply for the rest of the section.

Next we turn into the p_T distributions. We apply the previous cut of $\Delta R(j_1, \mu) > 0.4$. As we've already seen in 7.5.4, the p_T and in the electron case, the p_T distribution depends strongly on Δm , and we try to favor the low Δm acceptance in order to be more sensitive to it. The p_T distributions we see in 7.22 suggest a cut identical to the electron case of $p_T < 15 \text{ GeV}$. It is worth mentioning that the p_T of the muons are fed into the training of the Boosted Decision Tree (BDT) for further refinement, and therefore the exact value is being determined here quite loosely. The actual maximum value of the p_T of the muons will depend on the BDT cut being used to define the signal region.

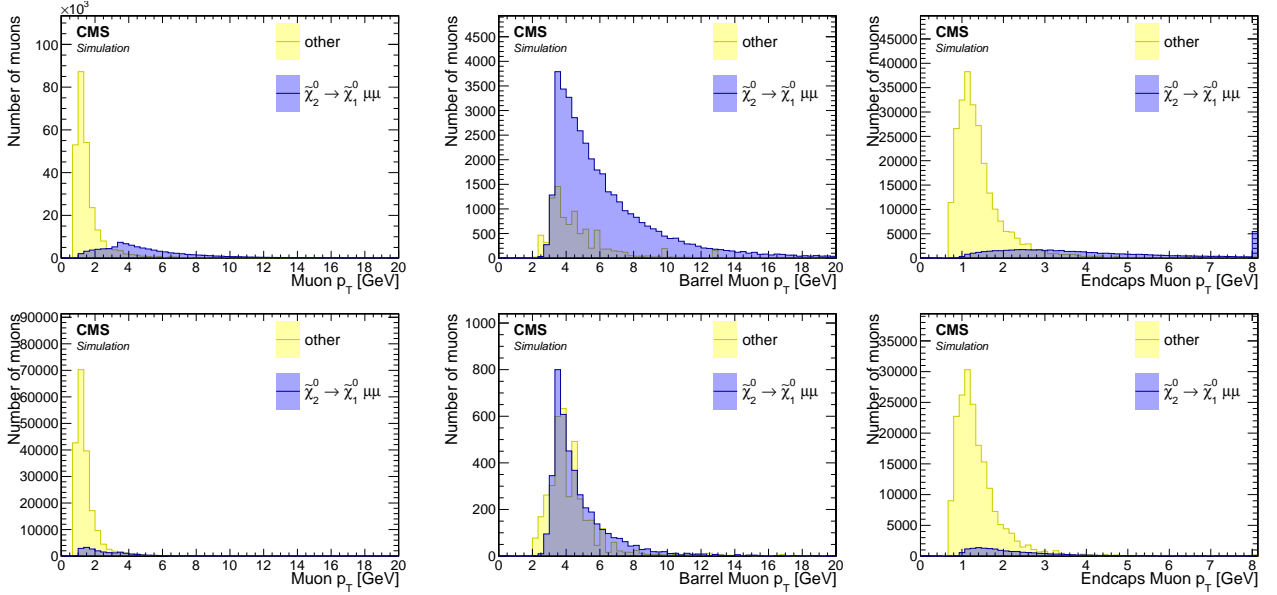


Figure 7.22: Reconstructed muons p_T distribution with loose ID for $\Delta m = 5.63$ GeV (top) and $\Delta m = 1.92$ GeV (bottom) in the inclusive case (left), barrel (middle) and endcaps (right). Cuts of $\Delta R(j_1, \mu) > 0.4$ and $p_T < 15$ GeV are applied.

We can see the point being made earlier about the endcaps being able to reconstruct muons with lower p_T , and therefore has worse purity than the barrel reiterated here. It must be stressed that worse purity is due to a much higher efficiency, and therefore, as long as we can purify it further, is not necessarily a bad thing. We see however, that the bulk of the non-signal muons populate the region of $p_T < 2$ GeV, and the ratio of signal muons to non-signal muons is very low in that region. We therefore make an additional cut of $p_T > 2$ GeV. Another way of looking at the effect of this cut is by looking at the $|\eta|$ distribution before and after the p_T cut which can be seen in 7.23.

We would like to see if requiring a tighter working point for the muon-identification is beneficial. The working point used in the previous distributions is loose. We look turn now to check the effects of requiring either a medium working point, or a tight one. We plot two bins labeled *fail* and *pass*, which correspond to whether the muon passes or failed the identification criteria of a medium or tight working points.

When we compare the medium working point in 7.24 to the tight working point in 7.25 we can see that the medium working point purifies the muons quite a lot and is very beneficial. However, when we look at the tight working point, we observe that we lose quite a lot of our wanted signal-muons without a significant gain in purity. We therefore choose to use the medium ID working point.

Our custom jet-isolation, which is described fully in 7.7.6, was devised mainly to reject SM background while retaining signal. In the electron case, we have seen in reffig:electrons-selection-isolation that it did a great job in also purifying the electron selection and replaced the need of requiring a tighter identification working point. In the case of the muons, we do rely on the a medium working point to perform this task, but we would like to also see the effects of the isolation on our signal muons. We see in 7.26 that we pay a small price by requiring the isolation, but we increase the sensitivity by rejecting a lot of SM background in the process.

We summaries this section with the full selection of the analysis muons:

- $2 < p_T < 15$ GeV
- $|\eta| < 2.4$
- $\Delta R(j_1, \mu) > 0.4$

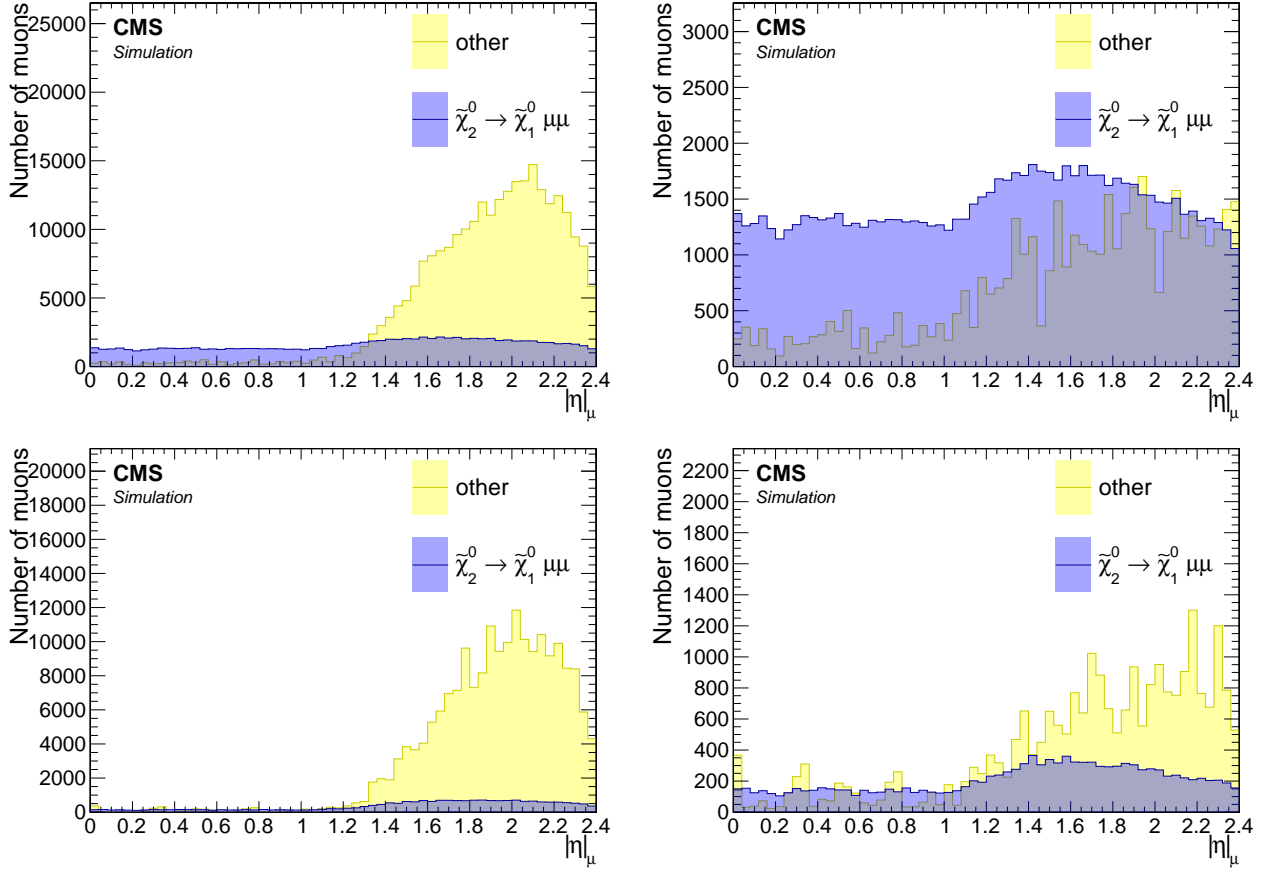


Figure 7.23: $|\eta|$ distribution of reconstructed muons with loose ID for $\Delta m = 5.63$ GeV (top) and $\Delta m = 1.92$ GeV (bottom) without (left) and with (right) $p_T > 2$ GeV cut. Cut of $\Delta R(j_1, \mu) > 0.4$ is also applied.

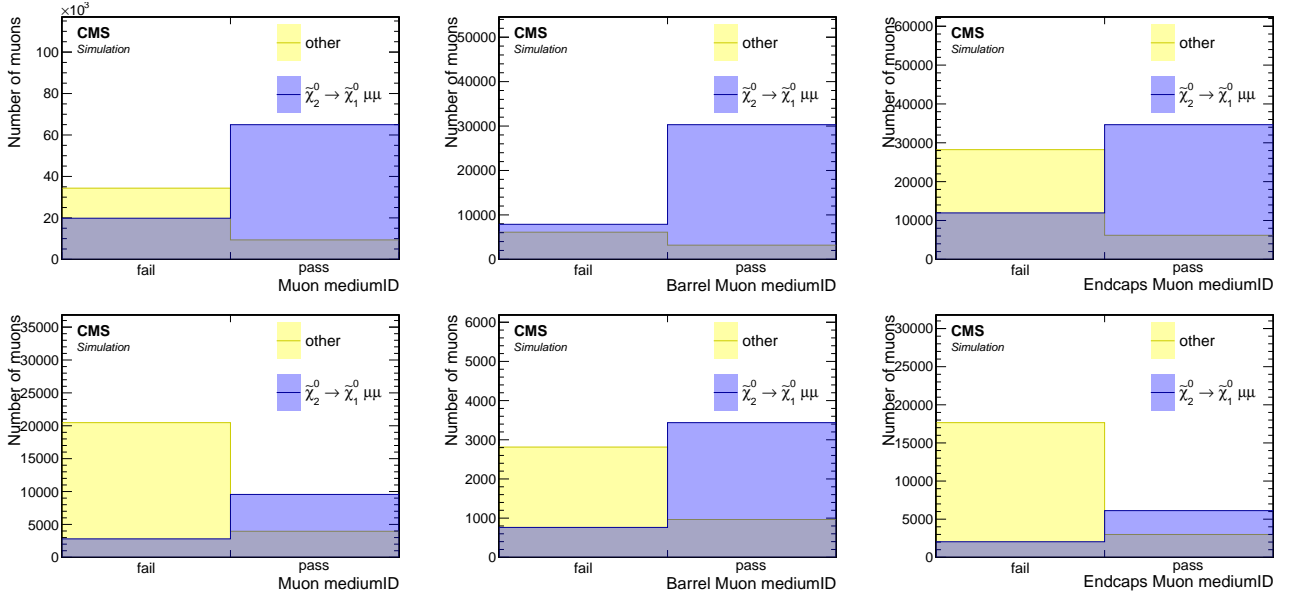


Figure 7.24: Medium ID working point distributions of reconstructed muons for $\Delta m = 5.63$ GeV (top) and $\Delta m = 1.92$ GeV (bottom) in the inclusive p_T case (left), barrel (middle) and endcaps (right). Cuts of $\Delta R(j_1, \mu) > 0.4$, $p_T > 2$ GeV and $p_T < 15$ GeV are applied.

- medium ID working point
- pass jet-isolation

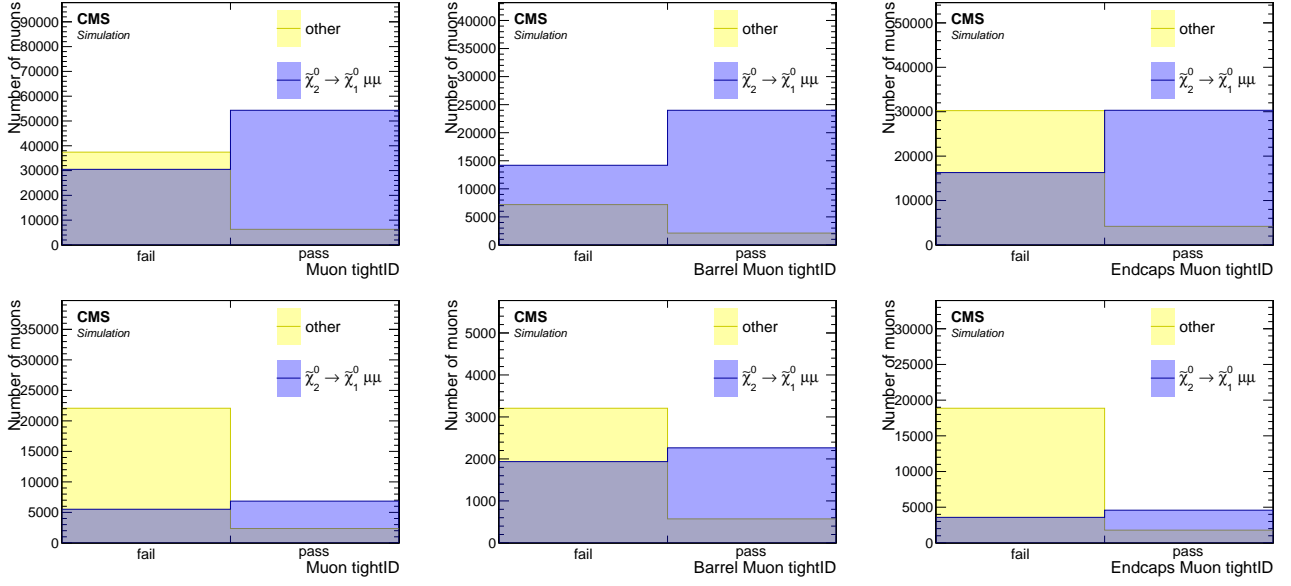


Figure 7.25: Tight ID working point distributions of reconstructed muons for $\Delta m = 5.63$ GeV (top) and $\Delta m = 1.92$ GeV (bottom) in the inclusive p_T case (left), barrel (middle) and endcaps (right). Cuts of $\Delta R(j_1, \mu) > 0.4$, $p_T > 2$ GeV and $p_T < 15$ GeV are applied.

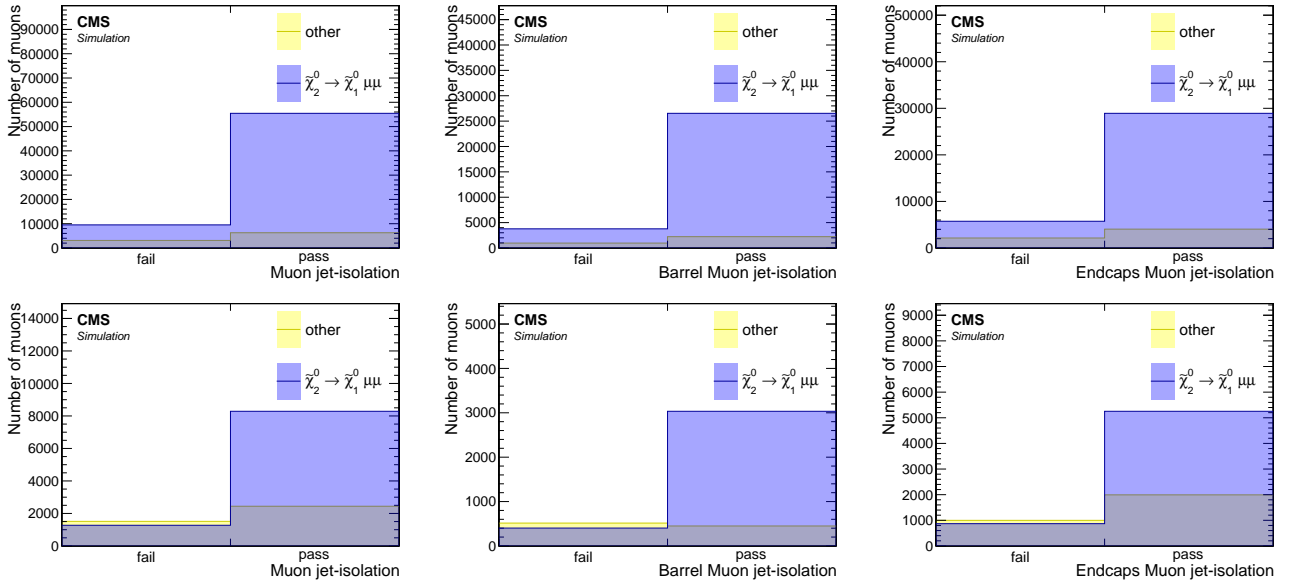


Figure 7.26: Jet-isolation distributions of reconstructed muons with medium ID for $\Delta m = 5.63$ GeV (top) and $\Delta m = 1.92$ GeV (bottom) in the inclusive p_T case (left), barrel (middle) and endcaps (right). Cuts of $\Delta R(j_1, \mu) > 0.4$, $p_T > 2$ GeV and $p_T < 15$ GeV are applied.

7.7.3 Scale factors

In 7.7.1 and 7.7.2 we have studied the selection we apply to electrons and muons respectively. We have therewith made a choice about identification working point. We have used simulation exclusively to draw conclusions about the identification efficiency of the leptons. If we rely on Monte Carlo (MC) simulation, that will produce large systematic errors due to imperfections in modeling both the data and the detector response. We therefore wish to measure the identification efficiency in data, in order to correct the simulation's potentially false efficiency rate. *Efficiency* is defined as how probable it is to reconstruct or identify a lepton. For a lepton ℓ the identification efficiency is defined as:

$$\varepsilon_{\ell}^{\text{ID}} = \frac{N_{\ell}(\text{ID})}{N_{\ell}(\text{produced})} \quad (7.1)$$

In MC simulation, the number of leptons produced is the same as the number of leptons generated. In data, one must measure it using a data-driven method. Once the efficiencies have been measured both in simulation and in data, a correction factor named Scale Factor (SF) can be applied to the simulation in order to correct for any discrepancies that might arise. The scale factors are defined as the ratio between the efficiency in data to the efficiency in simulation:

$$\text{SF}_{\ell}^{\text{ID}} = \frac{\varepsilon_{\ell}^{\text{ID,Data}}}{\varepsilon_{\ell}^{\text{ID,MC}}}, \quad (7.2)$$

dropping the superscript ID we get:

$$\text{SF}_{\ell} = \frac{\varepsilon_{\ell}^{\text{Data}}}{\varepsilon_{\ell}^{\text{MC}}}. \quad (7.3)$$

Once the relevant SF have been determined, they are applied for every lepton passing the object selection in the event. The scale factors for loose-ID electrons in our p_{T} range have been measured centrally by the relevant working group and are applied to the selected electrons. As was determined in 7.7.2, our analysis signal muon's lower p_{T} threshold is 2 GeV which is low. Scale factors for medium ID leptons with $p_{\text{T}} \geq 2$ GeV were computed centrally by the Muon Physics Object Group (POG). The scale factors, however, while matching our muons' p_{T} range and identification working point, were computed by requiring $\Delta R > 0.5$ between the muons [1, 2]. As we have seen in 7.5.4, one of the drivers of the sensitivity is the region of $\Delta R < 0.5$. We would therefore like to validate the scale factors in that region. We would like to show that the efficiencies have no ΔR dependence, and in order to do so, we calculate the efficiencies in different ΔR regions.

In order to measure such efficiency in data, one must identify desired leptons with low and easily reducible fakes. A widely used method to perform such a data-driven task is the Tag & Probe method. In the Tag & Probe method we examine a mass resonance such as Z, J/ ψ or Y to select particles of the desired type, and probe the efficiency of a particular selection criterion on those particles. The mass resonance will then decay into two same-flavor opposite charged pair of leptons and will form a peak on top of a background. Since we are interested in measuring the efficiency of low p_{T} muons, we choose to look at dimuon events around the J/ ψ mass window. In a dimuon event, we describe one muon as a 'tag' and the other as a 'probe'. The tag muon is selected with a very tight selection which results in very high certainty that the object corresponds to a real muon produced. The probe is given a loose selection, but since it is constrained to be consistent with a product of a J/ ψ , it is almost certain that originate from a real muon too. Since the shape of the J/ ψ is a peak over a background, the background is easily

removed by fits. The probe is then subjected to cuts or constraints which are used to measure a particular efficiency. As stated, in this study we want to show that the efficiency to identify a muon with medium ID working point from a track has no ΔR dependence. Therefore, the efficiency we are looking for is defined as:

$$\varepsilon_{\mu}^{\text{ID}} = \frac{N_{\mu}^{\text{ID}}}{N_t}. \quad (7.4)$$

The probe we are using in the denominator is a track passing a loose selection, while the probe track in the denominator is required to match a medium ID working point muon. The number of objects passing a selection is determined by a fit to data and MC, to measure the corresponding efficiencies in data and MC.

This study is done for year 2016. For the MC, we are using the 2016 samples listed in 7.6.1. For data, we are using a single electron trigger, in order for the tagged muon to be independent from the triggered object. The data set is measured to correspond to 36.02 fb^{-1} using the BRIL Work Suite [3]. The following trigger paths are used:

- HLT_Ele27_WPTight_Gsf_v*,
- HLT_Ele27_eta2p1_WPLoose_Gsf_v*,
- HLT_Ele32_WPTight_Gsf_v*,
- HLT_Ele35_WPTight_Gsf_v*.

We then select an offline loose ID electron with $p_T > 27 \text{ GeV}$ offline. The requirement to select a tag & probe pair are defined in table 7.7.3.

Table 7.3: Selection criteria for Tags and Probes

Tag	Probe
medium ID muon	isolated track
$p_T \geq 5 \text{ GeV}$	$2 \leq p_T \leq 20 \text{ GeV}$ ($p_T \geq 3 \text{ GeV}$ for barrel)
$ \eta < 2.4$	opposite-sign in invariant mass window $[2.5, 3.5] \text{ GeV}$

A fit is then performed in an invariant mass window around the J/ψ window of $[2.5, 3.5] \text{ GeV}$. The signal fit is using a crystal ball function and the continuum is fit with a 6th order polynomial. The fit is repeated twice, where the denominator is done with probe tracks, and the numerator is using medium ID muons that have been matched to said tracks. The ΔR range has been split into 3, and $|\eta|$ of the muons has been split into barrel ($|\eta| < 1.2$) and endcaps ($1.2 < |\eta| < 2.4$). Simulation fits are shown in 7.27 for barrel, and 7.28 for endcaps. Data fits are shown in 7.29 for barrel, and 7.30 for endcaps.

The efficiencies and corresponding scale factors can be seen in 7.31. The scale factors are statistically consistent with unity, and show no discernible ΔR dependence. A similar study has been carried out with simulation and data for 2017 and 2018 in [4] and did not observe a ΔR dependence either. The recommendation from the POG as a results of these studies are to use the calculated scale factors provided by them with an additional systematic of 1% for muons with $p_T < 20 \text{ GeV}$.

7.7.4 Missing transverse energy

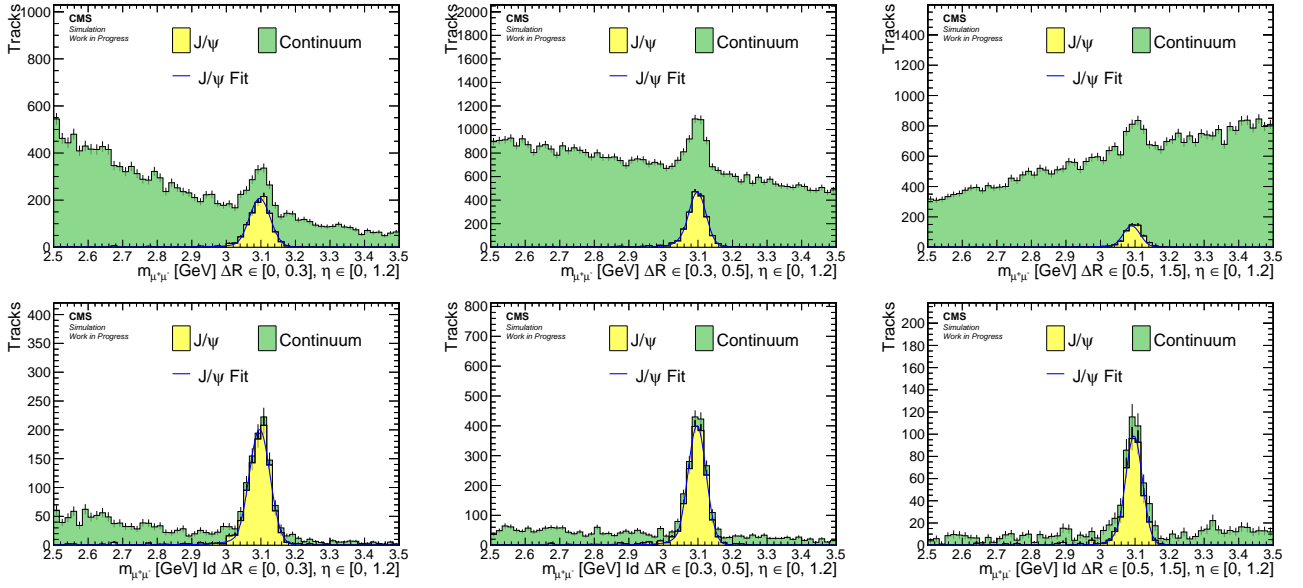


Figure 7.27: Simulation barrel muons fits for denominator (top) and numerator (bottom) for $0 < \Delta R < 0.3$ (left), $0.3 < \Delta R < 0.5$ (center), $0.5 < \Delta R < 1.5$ (right)

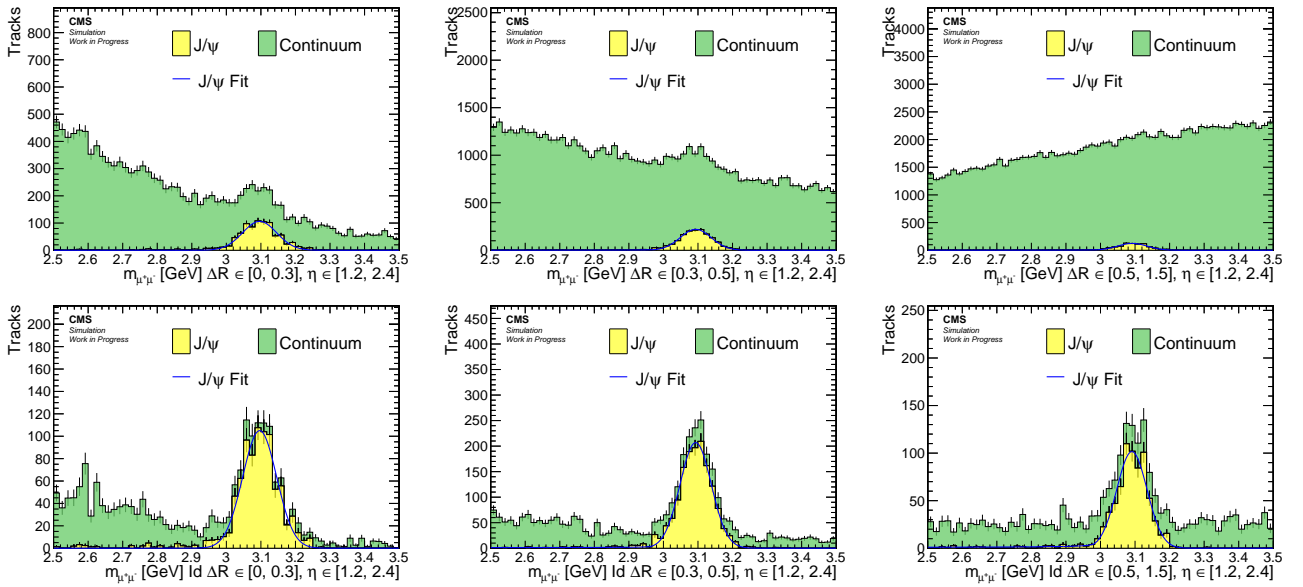


Figure 7.28: Simulation endcaps muons fits for denominator (top) and numerator (bottom) for $0 < \Delta R < 0.3$ (left), $0.3 < \Delta R < 0.5$ (center), $0.5 < \Delta R < 1.5$ (right)

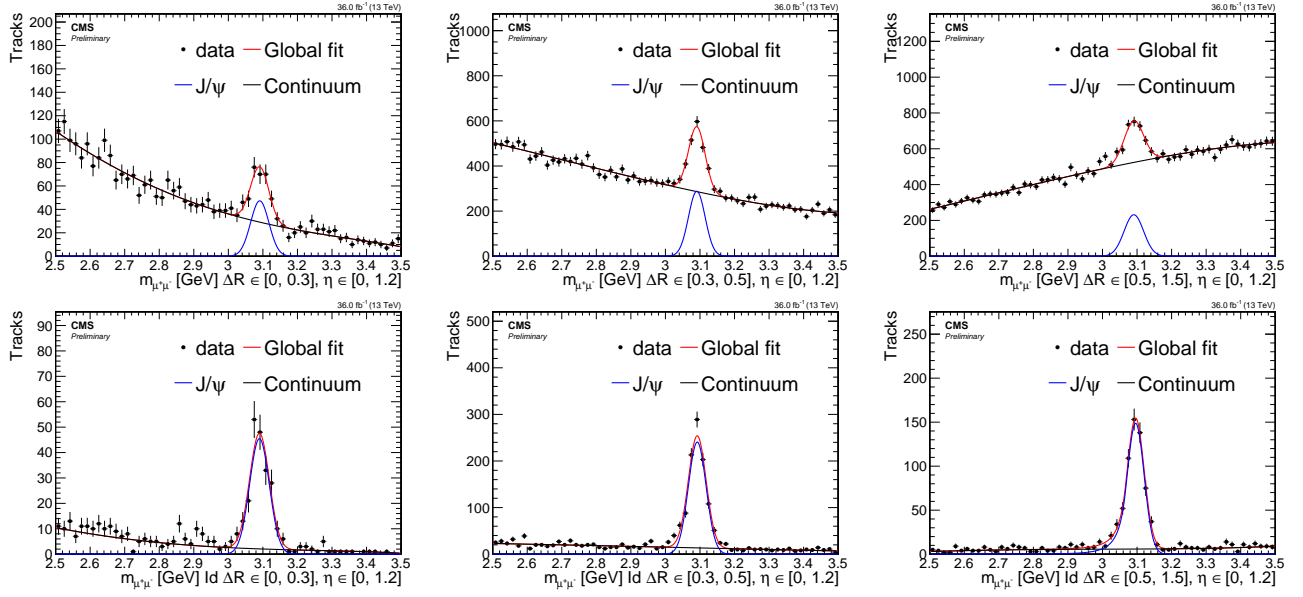


Figure 7.29: Data barrel muons fits for denominator (top) and numerator (bottom) for $0 < \Delta R < 0.3$ (left), $0.3 < \Delta R < 0.5$ (center), $0.5 < \Delta R < 1.5$ (right)

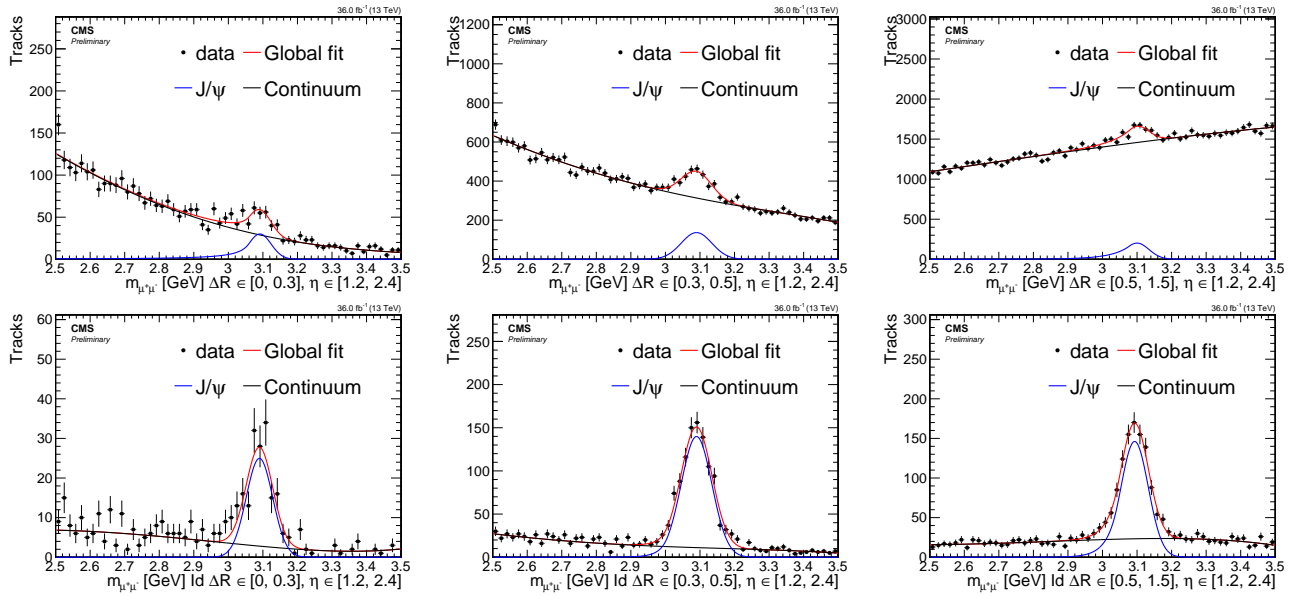


Figure 7.30: Data endcaps muons fits for denominator (top) and numerator (bottom) for $0 < \Delta R < 0.3$ (left), $0.3 < \Delta R < 0.5$ (center), $0.5 < \Delta R < 1.5$ (right)

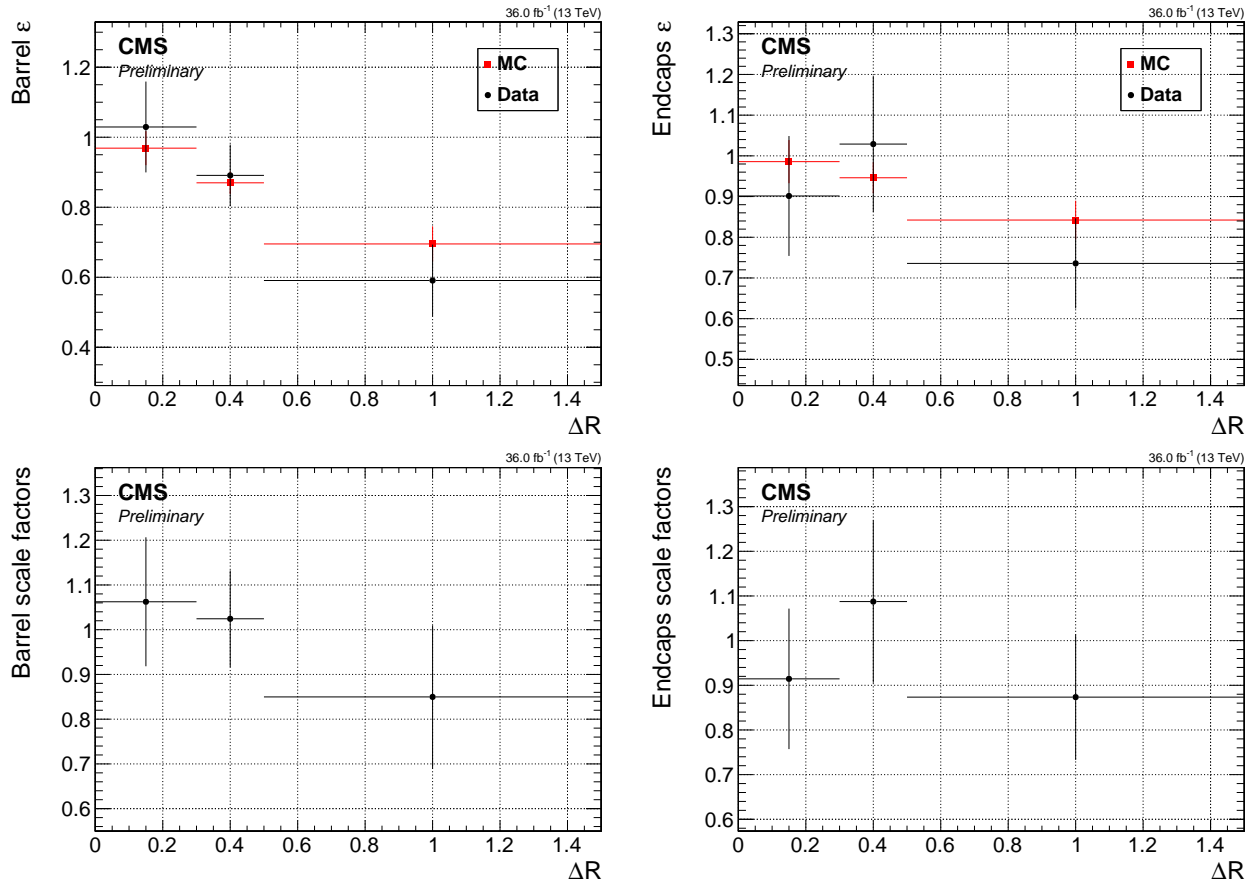


Figure 7.31: Efficiencies (top) and scale factors (bottom) for barrel muons (left) and endcaps muons (right).

7.7.5 Tracks and multivariate selection

The leptons $\ell^+\ell^-$ produced in our decay $\tilde{\chi}_2^0 \rightarrow \tilde{\chi}_1^0 \ell^+ \ell^-$ tend to have mostly very low transverse momentum p_T . We have seen in 6 that the identification and reconstruction of the muons get worst with lower p_T . Therefore, the aim of the exclusive track category is to try and regain lost leptons that didn't make the reconstruction or identification process. Since the tracking efficiency at our p_T ranges is well above 99%, as we've seen in 6.1, we can try and pick up the track that corresponds to our missing lepton by applying our knowledge about the event kinematics specific to our signal. We are therefore, not enhancing the lepton identification in the general case, but identifying missed tracks in our specific signal signature.

Since each event contains many tracks, we need a method to identify in the signal event, which track corresponds to our miss-identified lepton. In order to achieve this goal we train a Boosted Decision Tree (BDT). We train 4 BDTs which correspond to the lepton flavor, Muons or Electrons, and for each, we train separately for phase 0 (2016) and phase 1 (2017-2018) of the tracker. All BDTs use the same structure of 200 trees with a maximum depth of 3, with the TMVA package [5]. The BDT training is performed with AdaBoost and GiniIndex separation. We are taking all other values as the defaults set by the TMVA package.

For the training we take tracks from a pool of our privately produced FASTSIM signal simulations which were listed in 7.6.2. Of those, we are selecting the full range of simulated higgsino parameter μ (or the mass of $\tilde{\chi}_1^\pm$ in case of phase 1), but only the range of Δm we want to be most sensitive to. In phase 0, we select $\Delta m^0 \in [0.3, 4.3]$ GeV and $\mu \in [100 - 130]$ GeV. In phase 1 we select $\Delta m^\pm \in [0.3 - 4.6]$ GeV and $\mu \in [100 - 500]$ GeV. Those signal events we then split into signal tracks, i.e., tracks originating from the decay $\tilde{\chi}_2^0 \rightarrow \tilde{\chi}_1^0 \ell^+ \ell^-$ and been matched to the missing generated lepton in the generator level particles collection, and background tracks which do not match our wanted leptons. Therefore, our BDTs are useful to reject in-signal background of unwanted tracks. The samples for muons contain 9408 (10964) signal tracks and 99996 (151380) background tracks for phase 0 (phase 1). For electrons the samples contain 2364 (2288) signal tracks and 104065 (159713) background tracks for phase 0 (phase 1). The training samples are then tested against the test samples of equal size. The distributions of the testing samples overlay on the training samples are seen in 7.33.

A pre-selection is applied to all tracks in the collection obtained by the standard track reconstruction sequences. The pre-selection ensures a set of properly-reconstructed, isolated and prompt tracks, whose trajectories pass through the region nearby the primary vertex with the largest sum of charged-tracks, jets and missing energy values (PV):

- $p_T > 1.9$ GeV
- $|\eta| < 2.4$
- track $\text{iso}_{\text{rel}} < 0.1$, using $\Delta R(\text{track}, \text{other tracks}) < 0.3$
- $d_{xy}(\text{track}, \text{PV}) < 0.02$ cm w.r.t the PV
- $d_z(\text{track}, \text{PV}) < 0.02$ cm w.r.t the PV
- no match to an electron or muon within a cone of size 0.01

For the training we use 10 variables listed in decreasing order of their ranking (in the muon case of phase 0) listen in 7.7.5.

Distribution for the input variables showing the signal tracks in blue, and background tracks in red, are seen in 7.32.

Table 7.4: Track BDT input variables

Rank	Variable	Description
1	$\Delta R(t, \ell)$	t is the track and ℓ the lepton
2	$ \Delta\eta(t, \ell) $	
3	$p_T(\ell)$	
4	$ \Delta\phi(t, \vec{H}_T^{\text{miss}}) $	j_1 is the leading jet
5	$ \Delta\eta(t, j_1) $	
6	$ \Delta\phi(t, \ell) $	
7	$ \eta(t) $	invariant mass
8	$ \eta(\ell) $	
9	$\Delta R(\ell, j_1)$	
10	$m_{t\ell}$	

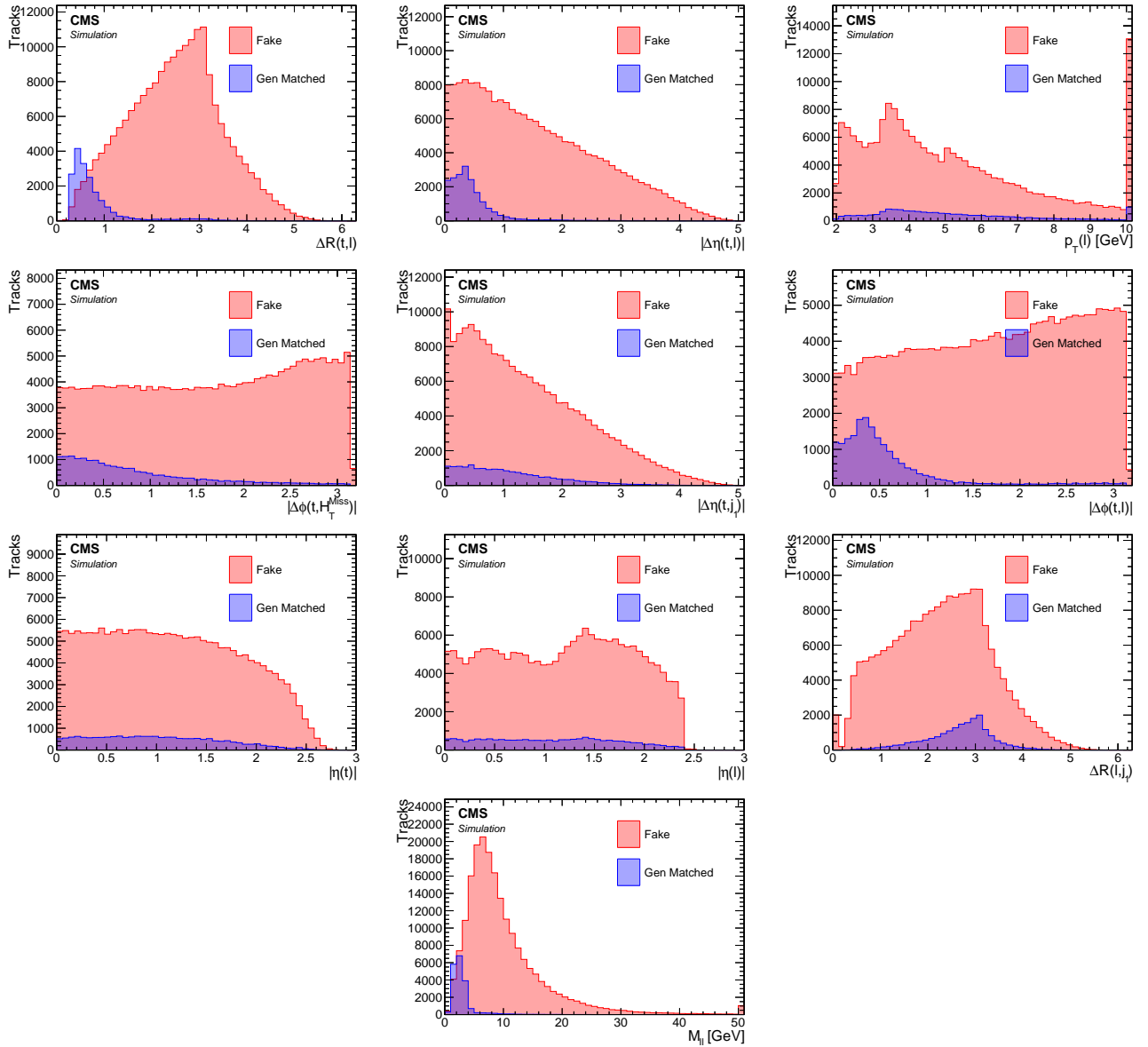


Figure 7.32: Distributions of the inputs for training for the track BDT in the Muon exclusive track category.

The output of the training of the 4 BDTs can be then seen in 7.33. The ROC curves are then plotted in 7.34. The red point shows the efficiency of the signal and background tracks of

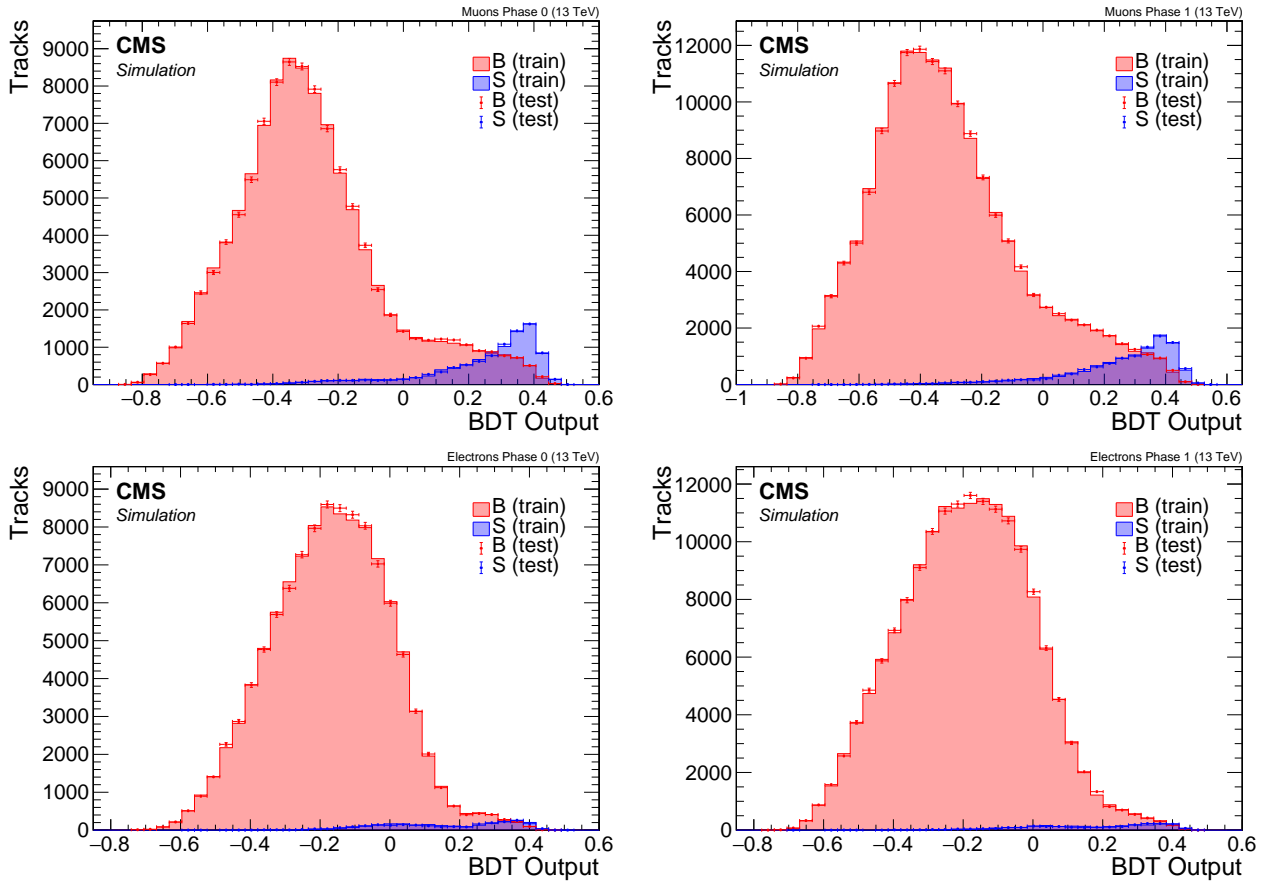


Figure 7.33: Track BDT output plots for Muons (top) and Electrons (bottom) in phase 0 (left) and phase 1 (right). Blue shows signal tracks, while Red are fake tracks. Test sample overlay on top of training sample.

the BDT cut chosen to be 0.0.

After the training process, we select the track with the maximum BDT score as our missing lepton in the event. We consider only events with a track with a score of greater than 0.0, which corresponds to the red dot in the ROC curves in 7.34.

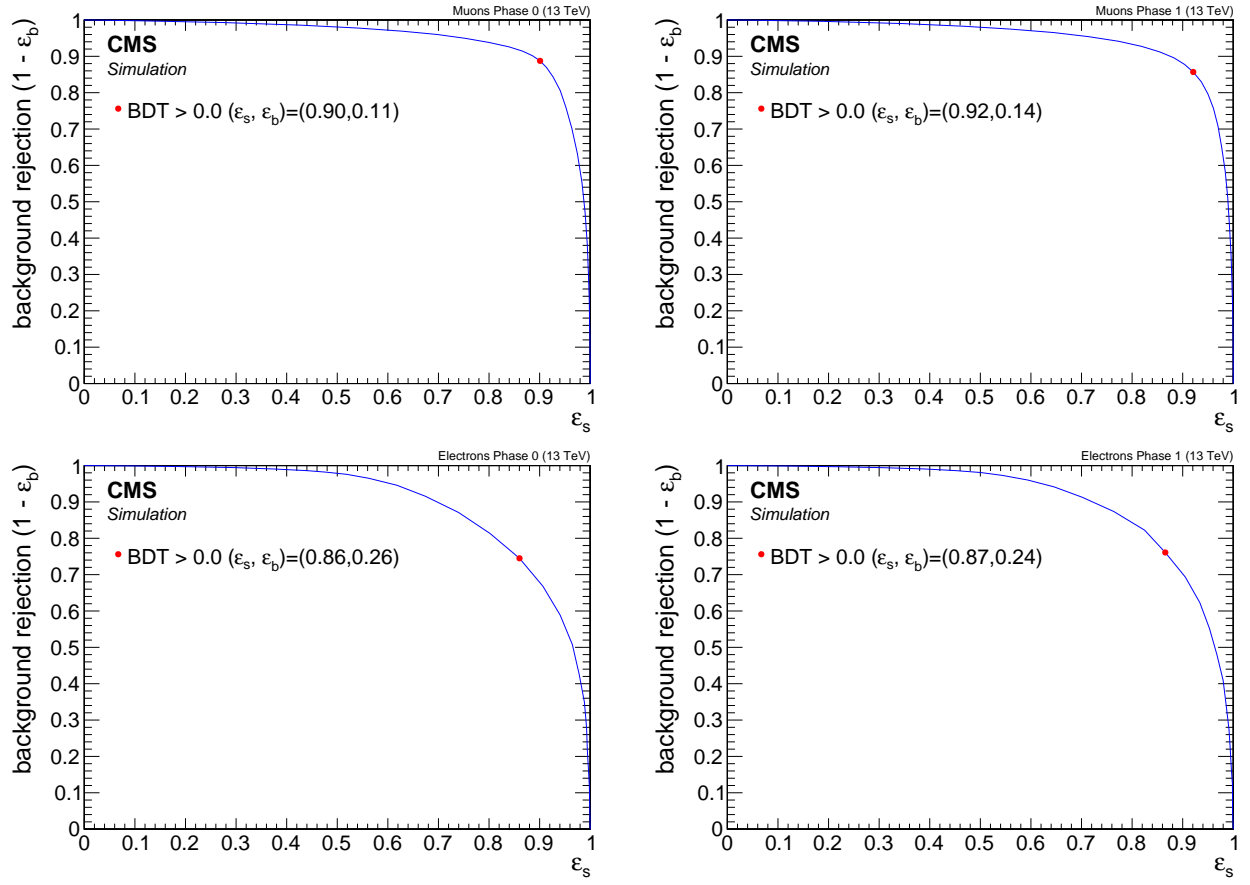


Figure 7.34: Track BDT ROC curves for Muons (top) and Electrons (bottom) in phase 0 (left) and phase 1 (right). Minimum working point showed as a red dot.

7.7.6 Isolation**7.8 Trigger****7.9 Event Selection****7.9.1 Preselection****7.9.2 High- p_T lepton veto****7.9.3 Selection Efficiencies****7.9.4 Boosted Decision Trees****7.10 Characterisation and Estimation of the Standard Model Backgrounds****7.11 Optimisation of Sensitivity****7.12 Results****7.13 Interpretation**

Chapter 8

Jet Isolation and Non-Isolated Background Estimation

8.1 Jet Isolation

8.1.1 Optimisation

8.2 Non-Isolated Background

Chapter 9

Summary

Chapter 10

Latex stuff

10.1 Some examples

10.1.1 Multiline comment

This is a line in introduction.

10.1.2 Fixme note

This is the introduction to the thesis. **FiXme Note: This is a fixme note** **FiXme Note: what** **FiXme Note: WHAT THE HELL AFTER**

10.1.3 Tables

h - here t - top b - bottom p - special page ! - even if not pretty

Table 10.1: Table captions are above the table whereas figure captions are below.

Parameter	Value 1	Value 2
s	10.0	20.0
t	20.0	30.0
u	30.0	40.0

10.1.4 Cross References

10.1.4 49 section 10.1.4

10.1.5 Particles

Hello World $\tilde{\chi}_1^0 \pi \eta_c$ GeV E_T^{miss} hey GeV E_T^{miss} π new one $\tilde{\chi}_1^0 \tilde{\chi}_1^0$

10.1.6 Citing

[6] SOS analysis

10.1.7 Glossary

Using glossary for computer computer plural form computers upper case first Computer upper case first plural Computers. To use for symbol π

10.1.8 Acronyms

First use of acronym SOS and second SOS. You can reset this and do again Soft-Opposite-Sign (SOS) and second time again SOS. Long version Soft-Opposite-Sign. Full version Soft-Opposite-Sign (SOS). Short version SOS.

List of Corrections

Note: fill in signal model stuff	13
Note: make sure we described both met and mht	15
Note: make sure we define the different deltaM somewhere	15
Note: add citation	15
Note: add citation and maybe reference to other section	15
Note: ref	16
Note: add ref	16
Note: ref	18
Note: ref	18
Note: ref	22
Note: cite	23
Note: This is a fixme note	49
Note: what	49
Note: WHAT THE HELL	49

Glossary

computer is a programmable machine that receives input, stores and manipulates data, and provides output in a useful format. 47

$\Delta\mathbf{m}$ mass difference between electroweakinos. If not explicitly said otherwise, it is the mass difference between $\tilde{\chi}_2^0$ and $\tilde{\chi}_1^0$, i.e., $\Delta\mathbf{m} = \Delta\mathbf{m}^0 = m_{\tilde{\chi}_2^0} - m_{\tilde{\chi}_1^0}$. 26, 27, 30

$\Delta\mathbf{m}^0$ mass difference between the neutral electroweakinos $\tilde{\chi}_2^0$ and $\tilde{\chi}_1^0$, i.e., $\Delta\mathbf{m}^0 = m_{\tilde{\chi}_2^0} - m_{\tilde{\chi}_1^0}$. 26

ΔR separation. 19, 23, 24

η pseudorapidity. 23

$E_{\mathbf{T}}^{\text{miss}}$ add description. 15, 16

$H_{\mathbf{T}}^{\text{miss}}$ add description. 15, 16

$m_{\ell\ell}$ invariant mass. 19–21

neutralino add description. 15, 16

ϕ azimuthal angle measured in radians. 23

π ratio of circumference of circle to its diameter. 47

$p_{\mathbf{T}}$ transverse momentum. 15, 16, 18, 19, 23, 26, 27, 30

Acronyms

- BDT** Boosted Decision Tree. 30, 39
- CERN** European Organization for Nuclear Research. 9
- CMS** Compact Muon Solenoid. 9
- DM** Dark Matter. 15
- ECAL** Electromagnetic Calorimeter. 27
- ISR** Initial State Radiation. 15, 16, 26, 27
- LHC** Large Hadron Collider. 9
- LSP** Lightest SUSY Particle. 15
- MC** Monte Carlo. 34, 35
- POG** Physics Object Group. 34, 35
- QCD** Quantum Chromodynamics. 15, 16
- SF** Scale Factor. 34
- SM** Standard Model. 15, 16, 23, 31
- SOS** Soft-Opposite-Sign. 21–24, 48
- SUSY** Supersymmetry. 15
- WIMP** Weakly Interacting Massive Particle. 15

Bibliography

- [1] https://gitlab.cern.ch/cms-muonPOG/MuonReferenceEfficiencies/-/tree/master/EfficienciesStudies/2016_legacy_rereco/Jpsi.
- [2] <https://indico.cern.ch/event/791428/contributions/3287172/attachments/1781977/2899551/2016LegacyReReco2.pdf>.
- [3] BRIL Group, “Bril work suite.”
<http://cms-service-lumi.web.cern.ch/cms-service-lumi/brilwsdoc.html>, 2017.
- [4] https://lguzzi.web.cern.ch/lguzzi/Tau3Mu/muonPOG_mediumID_dR.pdf.
- [5] A. Hoecker, P. Speckmayer, J. Stelzer, J. Therhaag, E. von Toerne, H. Voss, M. Backes, T. Carli, O. Cohen, A. Christov, D. Dannheim, K. Danielowski, S. Henrot-Versille, M. Jachowski, K. Kraszewski, A. Krasznahorkay, M. Kruk, Y. Mahalalel, R. Ospanov, X. Prudent, A. Robert, D. Schouten, F. Tegenfeldt, A. Voigt, K. Voss, M. Wolter, and A. Zemla, “Tmva - toolkit for multivariate data analysis,” 2007.
<https://arxiv.org/abs/physics/0703039>.
- [6] **CMS** Collaboration, A. Tumasyan *et al.*, “Search for supersymmetry in final states with two or three soft leptons and missing transverse momentum in proton-proton collisions at $\sqrt{s} = 13$ TeV,” *JHEP* **04** (2022) 091, [arXiv:2111.06296](https://arxiv.org/abs/2111.06296) [hep-ex].

List of Figures

7.1	Signal Models Feynman Diagrams	13
7.2	Signal E_T^{miss} and H_T^{miss} distributions	16
7.3	Signal <i>number of jets</i> and <i>leading jet</i> p_T distributions	17
7.4	Signal <i>number of b-tagged jets</i> distributions	17
7.5	Signal $\min \Delta\phi(E_T^{\text{miss}}, \text{jets})$ and $\min \Delta\phi(H_T^{\text{miss}}, \text{jets})$ distributions	18
7.6	Signal p_T distributions	19
7.7	Signal p_T distributions split into barrel and endcaps	20
7.8	Signal $ \eta $ distributions	20
7.9	Signal generator level $m_{\ell\ell}$ distributions	21
7.10	Signal $m_{\mu\mu}$ vs. p_T	22
7.11	Signal reconstructed $m_{\mu\mu}$	22
7.12	Signal generator level ΔR distributions	23
7.13	Signal $\Delta R(\mu\mu)$ vs. p_T	24
7.14	Signal reconstructed $\Delta R(\mu\mu)$	24
7.15	Spatial separation between reconstructed electrons and the leading jet $\Delta R(j_1, e)$	26
7.16	p_T distribution of reconstructed electrons with loose ID	27
7.17	$ \eta $ distribution of reconstructed electrons with loose ID	27
7.18	medium and tight ID working points distribution of reconstructed electrons	28
7.19	standard isolation and jet-isolation distribution of reconstructed electrons	29
7.20	$ \eta $ distribution of reconstructed electrons with loose ID passing jet-isolation	29
7.21	Spatial separation between reconstructed muons and the leading jet $\Delta R(j_1, \mu)$	30
7.22	Reconstructed muons p_T	31
7.23	$ \eta $ distribution of reconstructed muons with loose ID before and after $p_T > 2 \text{ GeV}$ cut	32
7.24	medium ID working point distribution of reconstructed muons	32
7.25	tight ID working point distribution of reconstructed muons	33
7.26	jet-isolation distribution of reconstructed muons	33
7.27	Simulation barrel muons fits	36
7.28	Simulation endcaps muons fits	36
7.29	Data barrel muons fits	37
7.30	Data endcaps muons fits	37
7.31	Efficiencies and scale factors	38
7.32	Muon track BDT training inputs	40
7.33	Track BDT output plots	41
7.34	Track BDT ROC curves	42

List of Tables

7.1	Base selection applied to all analysis categories	18
7.2	Generator level efficiency on muons selections	21
7.3	Selection criteria for Tags and Probes	35
7.4	Track BDT input variables	40
10.1	Table captions are above the table whereas figure captions are below.	49